SANDIA REPORT
SAND2008-7655
Unlimited Release
Printed November 2008

Fundamental Materials Issues for Thermochemical H_2O and CO_2 Splitting

Final Report (FY08)

Eric N. Coker, Mark A. Rodriguez, Andrea Ambrosini, Roland R. Stumpf, Ellen B. Stechel, Chris Wolverton and Bryce Meredig

Prepared by
Sandia National Laboratories
Albuquerque, New Mexico 87185 and Livermore, California 94550

Sandia is a multiprogram laboratory operated by Sandia Corporation,
a Lockheed Martin Company, for the United States Department of Energy's
National Nuclear Security Administration under Contract DE-AC04-94AL85000.

Issued by Sandia National Laboratories, operated for the United States Department of Energy by Sandia Corporation.

Available to DOE and DOE contractors from
U.S. Department of Energy
Office of Scientific and Technical Information
P.O. Box 62
Oak Ridge, TN 37831

Telephone: (865) 576-8401
Facsimile: (865) 576-5728
E-Mail: reports@adonis.osti.gov
Online ordering: http://www.osti.gov/bridge

Available to the public from
U.S. Department of Commerce
National Technical Information Service
5285 Port Royal Rd.
Springfield, VA 22161

Telephone: (800) 553-6847
Facsimile: (703) 605-6900
E-Mail: orders@ntis.fedworld.gov
Online order: http://www.ntis.gov/help/ordermethods.asp?loc=7-4-0#online

SAND2008-7655
Unlimited Release
Printed November 2008

Fundamental Materials Issues for Thermochemical H_2O and CO_2 Splitting

Final Report (FY08)

Eric N. Coker, Mark A. Rodriguez, Andrea Ambrosini, Roland R. Stumpf and Ellen B. Stechel
Sandia National Laboratories
P.O. Box 5800
Albuquerque, NM 87185-1349

Chris Wolverton and Bryce Meredig
Department of Materials Science & Engineering
Northwestern University
Evanston, IL 60208

Abstract

Hydrogen and carbon monoxide may be produced using solar-thermal energy in two-stage reactions of water and carbon dioxide, respectively, over certain metal oxide materials. The most active materials observed experimentally for these processes are complex mixtures of ferrite and zirconia based solids, and it is not clear how far the ferrites, the zirconia, or a solid solution between the two participate in the change of oxidation state during the cycling. Identification of the key phases in the redox material that enable splitting is of paramount importance to developing a working model of the materials. A three-pronged approach was adopted here: computer modeling to determine thermodynamically favorable materials compositions, bench reactor testing to evaluate materials' performance, and in-situ characterization of reactive materials to follow phase changes and identify the phases active for splitting. For the characterization and performance evaluation thrusts, cobalt ferrites were prepared by co-precipitation followed by annealing at 1400 °C.

An in-situ X-ray diffraction capability was developed and tested, allowing phase monitoring in real time during thermochemical redox cycling. Key observations made for an un-supported cobalt ferrite include: 1) ferrite phases partially reduce to wustite upon heating to 1400 °C in helium; 2) exposing the material to air at 1100 °C causes immediate re-oxidation; 3) the re-oxidized material may be thermally reduced at 1400 °C under inert; 4) exposure of a reduced material to CO_2 results in gradual re-oxidation at 1100 °C, but minimization of background O_2-levels is essential; 5) even after several redox cycles, the lattice parameters of the ferrites remain constant, indicating that irreversible phase separation does not occur, at least over the first five

cycles; 6) substituting chemical (hydrogen) reduction for thermal reduction resulted in formation of a CoFe metallic alloy.

Materials were also evaluated for their CO_2-splitting performance in bench reactor systems utilizing chemical reduction in place of thermal reduction. These tests lead to the following general conclusions: 1) despite over-reduction of the cobalt ferrite phase to CoFe alloy on chemical reduction, splitting of CO_2 still occurs; 2) the kinetics of chemical reduction follow the sequence: un-supported < ZrO_2-supported < yttria-stabilized ZrO_2 (YSZ)-supported ferrite; 3) ferrite/YSZ re-oxidizes faster than ferrite/ZrO_2 under CO_2 in the range 400 – 700 °C.

The temperature and pressure regimes in which the thermal reduction and water-splitting steps are thermodynamically favorable in terms of the enthalpy and entropy of oxide reduction, were determined. These metrics represent a useful design goal for any proposed water-splitting cycle. Applying this theoretical framework to available thermodynamic data, it was shown that none of the 105 binary oxide redox couples that were screened possess both energetically favorable reduction and oxidation steps. However, several driving forces, including low pressure and a large positive solid-state entropy of reduction of the oxide, have the potential to enable thermodynamically-favored two-step cycles.

Table of Contents

List of Figures

Figure 3. Stacked plot of XRD intensities as function of temperature (left) and environment (right). The indicated O_2 concentration downstream of the sample cell is included. Thermal reduction under He; re-oxidation under CO_2. For simplicity, cobalt is omitted from the labels.

Figure 4. XRD patterns extracted from Figure 3 illustrating fast and slow oxidation processes on switching from He flow (scan Q) to CO_2 flow (scans R – V).

Figure 5. Stacked plot of XRD intensities as function of temperature (left) and environment (right). The indicated O_2 concentration downstream of the sample cell is included. Thermal reduction under He; re-oxidation under CO_2 (at low temperature). For simplicity, cobalt is omitted from the labels.

Figure 6. XRD patterns of reactive materials before (A) and after various thermochemical cycles (B – D). Sample B: thermally reduced 1400 °C; re-oxidized in air, 1100 °C. Sample C: thermally reduced 1400 °C; re-oxidized in CO_2 with high O_2-content, 1100 °C. Sample D: thermally reduced 1400 °C; re-oxidized in CO_2 with lower O_2-content, 1100 °C.

Figure 7. (a)XRD patterns of reactive materials heated to 600 °C under He (first two patterns) and after contact with 3% H_2 at 600 °C (remaining patterns). (b) TGA of $Co_{0.95}Fe_{2.05}O_4$ under forming gas (%5H_2 inAr) showing conversion to CoFe alloy.

Figure 8. TPR curves of ferrites after oxidation at 600 °C under air. Reduction is measured as a mass loss due to the extraction of oxygen from the ferrite. Reduction under 5 % H_2/N_2 at a ramp rate of 2 °C min^{-1} (A) and 0.25 °C min^{-1} (B), followed by 30 minute hold at 700 °C. Mass data are normalized to the ferrite fraction in the mixture.

Figure 9. Bench reactor evaluation of un-supported $Co_{0.67}Fe_{2.33}O_4$ at 600 °C. For the first 30 minutes the reactor was bypassed to verify the composition of the feed gas (nominal 3% CO_2 in N_2). Shaded areas represent period of exposure to gases indicated at bottom; un-shaded areas = inert purge. Space velocity during CDS = 2100 ml_{gas} $ml_{ferrite}^{-1}$ $hour^{-1}$.

Figure 10. Bench reactor evaluation of un-supported $Co_{0.67}Fe_{2.33}O_4$ at 600 – 750 °C under 3% CO_2. For first 45 minutes reactor was bypassed to verify composition of feed gas (nominal 3% CO_2 in N_2). Space velocity = 2100 ml_{gas} $ml_{ferrite}^{-1}$ $hour^{-1}$.

Figure 11. TEOM evaluation of $Co_{0.67}Fe_{2.33}O_4$ supported on ZrO_2 and YSZ during temperature/redox cycling. Reduction temperature (T_R) = 400 °C, re-oxidation temperature (T_{OX}) = 600 °C. Each step in cycle (see inset) ~ 10 minutes. Mass data are normalized to the ferrite fraction in the mixture.

Figure 12: TGA of $Co_{0.95}Fe_{2.05}O_4$ under reduction conditions and simulated water (top) and CO_2 (bottom) splitting reactions.

List of Tables

Table 1. Phase composition and lattice parameters from XRD after thermochemical cycling.

INTRODUCTION

Thermochemical cycles using metal oxides with the spinel structure (AFe_2O_4; also called ferrites) are a promising method for producing hydrogen using solar energy to drive a two-step water-splitting cycle.[1,2] These cycles consist of a thermal reduction step (TR; reaction (1)) in which solar thermal energy is used to reduce the Fe^{III} to the Fe^{II} state with release of O_2, followed by a water splitting step (WS; reaction (2)) in which the reduced oxide reacts with steam to form hydrogen and regenerate the ferrite:

$$A_xFe_{3-x}O_4 \xleftrightarrow{\Delta} xAO + (3-x)FeO + 0.5\ O_2 \quad (1)$$

$$xAO + (3-x)FeO + H_2O \xleftrightarrow{\Delta} A_xFe_{3-x}O_4 + H_2 \quad (2)$$

Reactions (1) and (2) represent only the redox processes involving stoichiometric compounds, while in fact solid solutions are formed in (1) that are composed of various metal oxides. In the simplest case, A = Fe and the redox system comprises the reduction of iron ferrite (magnetite) to ferric oxide (wustite). Hydrogen production using Fe_3O_4, originally proposed by Nakamura,[3] is not practical, since the temperatures required to drive the TR step (2100 K) result in sintering of the material or formation of a liquid phase, leading to loss of oxide by vaporization and irreversibility. Supporting Fe_3O_4 on yttria-stabilized zirconia (YSZ) reduces this problem,[4,5] and in some cases supported ferrites have been found to improve in performance over many cycles.[6] Alternative redox systems, in which A is either a transition metal or and alkaline earth, have been proposed to decrease the temperature required for TR. These mixed-metal ferrites, including the systems with A = Mn[7], Co[8], Ni[9,10], and Zn[11,12] are now receiving considerable attention, and been recently reviewed.[13] The TR (reaction (1)) can be driven at temperatures of 1650 – 1950 K (i.e., is achievable using concentrated solar-thermal energy), while the WS (reaction 2) equilibrium is favored at lower temperatures. There is, however, a trade off between equilibrium and kinetics; below a certain temperature the kinetics of reaction (2) are prohibitively slow. A compromise is achieved in the range 1350 – 1500 K where hydrogen yields are maximized. The need for large temperature swings as well as spatial/temporal isolation of the TR and WS reactions (to avoid energetic re-combination of O_2 and H_2) was addressed at Sandia in the design of the CR5 reactor, described elsewhere.[14]

As outlined recently by Miller[15], the analogous thermochemical cycle involving splitting of carbon dioxide (CDS) into oxygen and carbon monoxide as a route to synthetic fuels may have some advantages over that of WS, based upon thermodynamics. The simplified reaction scheme for thermochemical CDS is described by a combination of reaction (1) above, and reaction (3) thus:

$$xAO + (3-x)FeO + CO_2 \xleftrightarrow{\Delta} A_xFe_{3-x}O_4 + CO \quad (3)$$

Once either CO or H_2 is formed, the well-known water-gas shift reaction (4) or reverse water-gas shift reaction (5) may be utilized to produce a mixture of CO and H_2 (syngas), a key step in producing synthetic fuels.

$$CO + H_2O \rightarrow CO_2 + H_2 \quad (4)$$

$$CO_2 + H_2 \rightarrow CO + H_2O \quad (5)$$

This project aimed to develop the first principles computational capability including experimental validation for complex metal oxide solid solutions, such as redox oxides used for WS and CDS. While the modeling addressed both WS and CDS, the experimental work focused on CDS.

EXPERIMENTAL SECTION

Materials synthesis

Cobalt ferrite-based materials active for WS and CDS were prepared via conventional co-precipitation from a solution of iron nitrate and cobalt nitrate by addition to an ammonia solution. The obtained powders were washed and dried, then calcined in air to 1100 °C. For experiments where the cobalt ferrite was to be supported, the calcined powder was physically mixed with either zirconia (ZrO_2) or yttria-stabilized zirconia (YSZ, 3% Y in ZrO_2). The mass ratio of ferrite : support was kept constant at 1 : 3 for this project. The mixture (or pure ferrite) was then pressed into a self-supporting disc using an IR pellet press (5 tonnes, 30 secs), was broken up and ground in a mortar and pestle, then sieved to collect the 40/60 mesh size fraction. The 40/60 fraction was then re-calcined to 1400 °C in air prior to evaluation. For characterization by XRD, powder samples were calcined as above, without pressing, crushing, and sieving.

Phase monitoring in-situ

In situ X-ray Diffraction (XRD) experiments were conducted using a modified X-ray diffractometer with controlled atmosphere (static, or dynamic flow, vacuum to ambient pressure), high temperature (ambient to 1450 °C) sample cell (Figure 1). In order to provide adequate control of background oxygen levels, a getter furnace was positioned upstream of the sample cell, and an O_2-meter was positioned at the exit of the cell. The getter furnace was bypassed during CO_2 flow, to avoid damage to the getter catalyst. An O_2-absorbing purifier bed specifically designed for CO_2 streams was used in later experiments; it was positioned immediately downstream of the CO_2 regulator (not shown in Figure 1). All pipework, valves, etc. upstream of the XRD sample cell were metal, in order to minimize ingress of oxygen (O_2 can diffuse through plastic tubing at a rate high enough to have an effect on the results of the splitting reactions). The modified XRD system allowed phase identification during the entire thermochemical cycle.

Materials evaluation

Bench reactor tests were carried out in either a quartz tube reactor (max. temperature 1000 °C), or in a Tapered Element Oscillating Microbalance - Pulse Mass Analyzer (TEOM Series 1500 PMA, Rupprecht & Patashnick, max. temperature 700 °C). Since the maximum temperatures achievable in these reactors were below that needed for efficient TR of the cobalt ferrites, chemical reduction was employed using dilute hydrogen. Tube reactor tests were conducted isothermally, since the thermal mass of the reactor system was too high to allow thermal cycling on a meaningful timescale. The TEOM, however, is capable of rapid thermal swings (e.g., 400 – 700 °C and 700 – 400 °C each in < 10 mins). In-line micro-GCs monitored the product gas stream for CO, CO_2 concentrations, while in the TEOM the mass of the sample was monitored in real time during oxidation/reduction cycling.

Thermogravimetric Analysis/Differential Thermal Analysis (TGA/DTA) was performed on a TA Instruments Q600 SDT. Powder samples of $Co_{0.95}Fe_{2.05}O_4$ were run under simulated solar reduction conditions (Ar/1400 ºC) and oxidizing conditions (air, CO_2, or H_2O/1100 ºC).

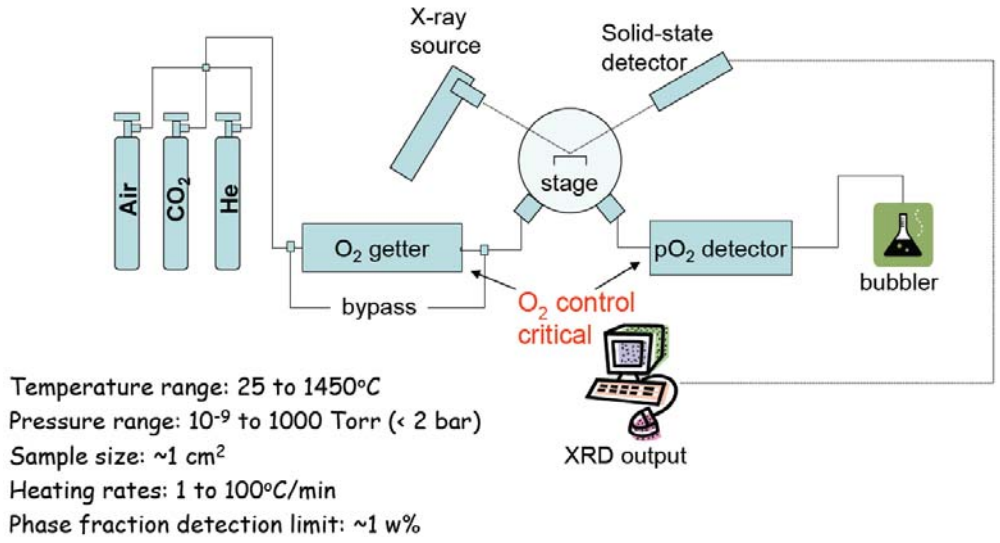

Figure 1. Schematic diagram of in situ XRD setup.

RESULTS

A) In-situ phase monitoring via high-temperature, controlled-atmosphere XRD

The XRD experiments used a cobalt ferrite with nominal composition $Co_{0.95}Fe_{2.05}O_4$ (hereafter referred to as $CoFe_2O_4$ for simplicity) which was not supported on ZrO_2 or YSZ in order to simplify phase identification for these initial trials.

Ramping the temperature from ambient to 1400 °C under helium resulted in partial reduction of $CoFe_2O_4$ to Co_xFe_yO (x + y = 1). The reduction was first noticed at 1200 °C, and on cooling the sample to 1100 °C, the reduced form persisted. Introduction of air at 1100 °C caused immediate re-oxidation of the material to $CoFe_2O_4$; subsequent purging with helium and re-heating to 1400 °C reformed the Co_xFe_yO phase. A stacked plot of representative XRD peak intensities (brighter = higher intensity) recorded during this experiment is shown in Figure 2. The peak position of the alumina sample holder provides an internal temperature calibration.

Repeating the above experiment, but introducing CO_2 at 1100 °C instead of air resulted in a more gradual re-oxidation of the material, as shown in Figure 3. For this experiment the CO_2 was not purified to remove trace O_2 (an estimated maximum of 80 ppm O_2 may have been present). The individual XRD patterns in Figure 4 illustrate the presence of two competing oxidation pathways. The XRD pattern labeled Q was recorded immediately before He flow was changed to CO_2 flow, and each subsequent pattern was recorded at approximately 6 minute increments. In pattern Q, both ferrite and wustite phases were observed. During scan R, however, a rapid oxidation process appeared to be taking place: the diffraction peak for wustite

at 36.3 °2Θ was observed at similar intensity to scan Q, but ~ 2 minutes later, the wustite peak at 42 °2Θ had disappeared. In subsequent scans, the intensity of the 36.3 °2Θ peak gradually diminished, indicative of the slow re-oxidation process. The rapid oxidation may be attributed to a surface reaction, whereas the slower oxidation was a bulk process. It is also possible that a small leak allowed ingress of air to the gas lines prior to initiating CO_2 flow, creating a short pulse of O_2 and contributing to the initial fast re-oxidation. Future experiments, employing CO_2 of minimal O_2-content will possibly enable better differentiation of the surface ("fast") versus bulk ("slower") reactions.

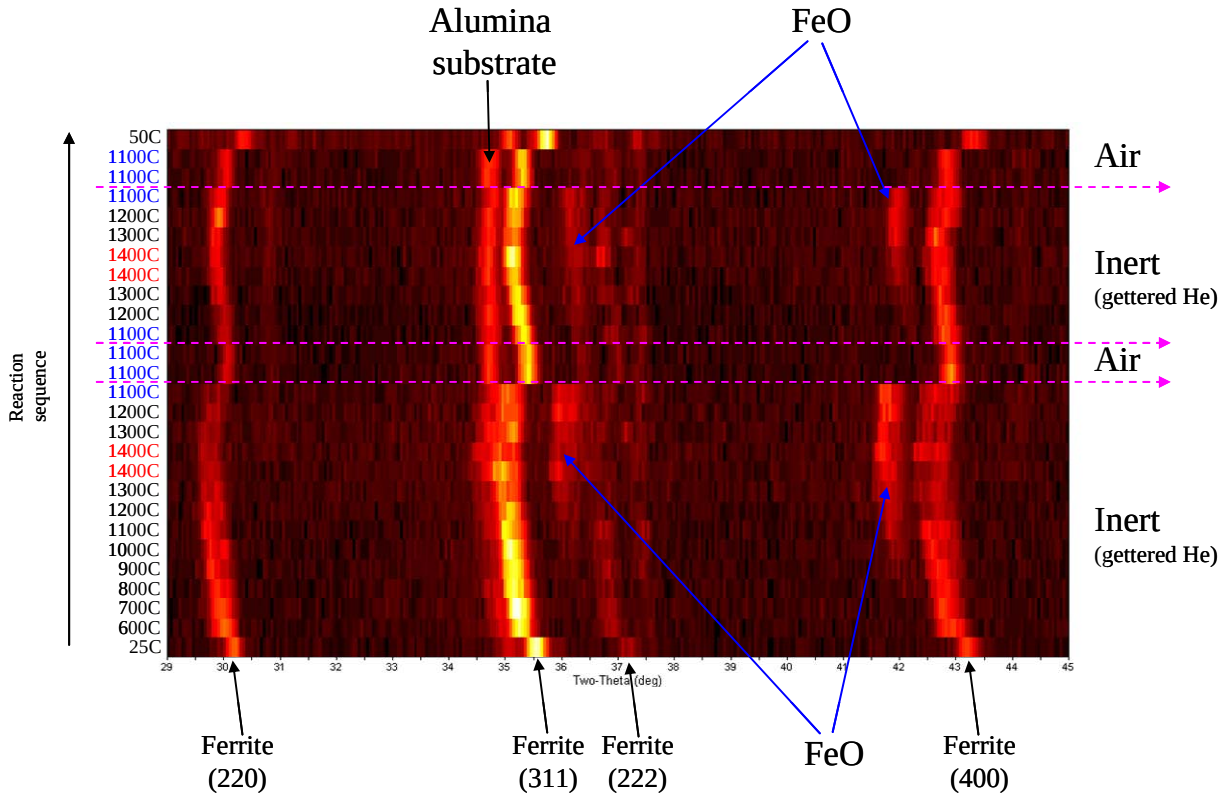

Figure 2. Stacked plot of XRD intensities as a function of temperature (left) and environment (right). Thermal reduction under He; re-oxidation under air. For simplicity, cobalt is omitted from the labels.

Furthermore, it is apparent from the observed oxygen concentrations (Figure 3), that a small quantity of O_2 may have been desorbed from the material during thermal reduction at 1400 °C (as is expected from reaction (1)). At temperatures below 1300 °C, no O_2 was detected, but at 1400 °C, 0.1 ppm O_2 (limit of detection) was observed.

In order to slow the kinetics of re-oxidation, an experiment was performed where reduction occurred at 1400 °C, then the sample cell was cooled to 600 °C under inert gas prior to beginning the CO_2 flow. In this case, the CO_2-purifier was used to remove trace O_2. As is seen from Figure 5, the re-oxidation to the ferrite phase was a gradual process, and no obvious fast re-oxidation was observed. The latter observation is more likely due to the reduction of O_2-background than to the lower temperature, since oxidation by O_2 is still rapid at 600 °C. A suspected malfunction in the oxygen analyzer during this experiment renders uncertainty in the oxygen concentrations shown in Figure 5; therefore these will not be discussed.

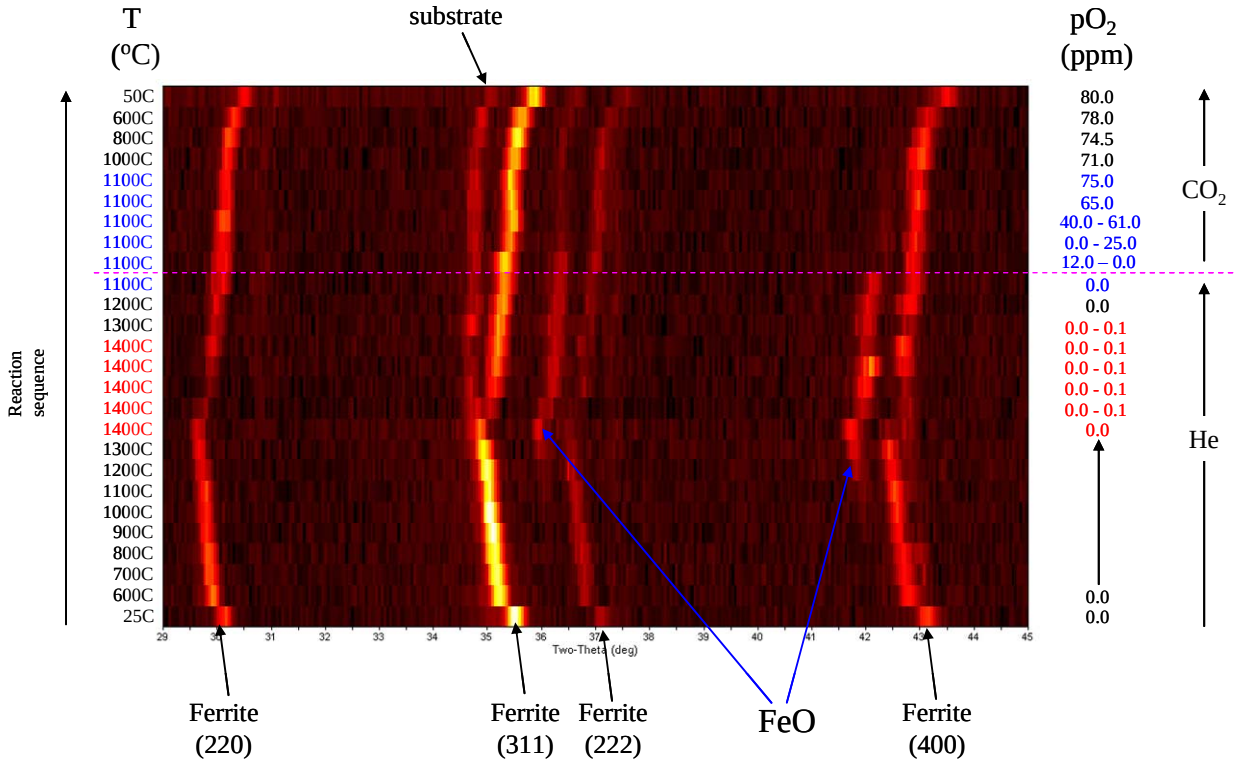

Figure 3. Stacked plot of XRD intensities as function of temperature (left) and environment (right). The indicated O_2 concentration downstream of the sample cell is included (malfunction renders these values questionable). Thermal reduction under He; re-oxidation under CO_2. For simplicity, cobalt is omitted from the labels.

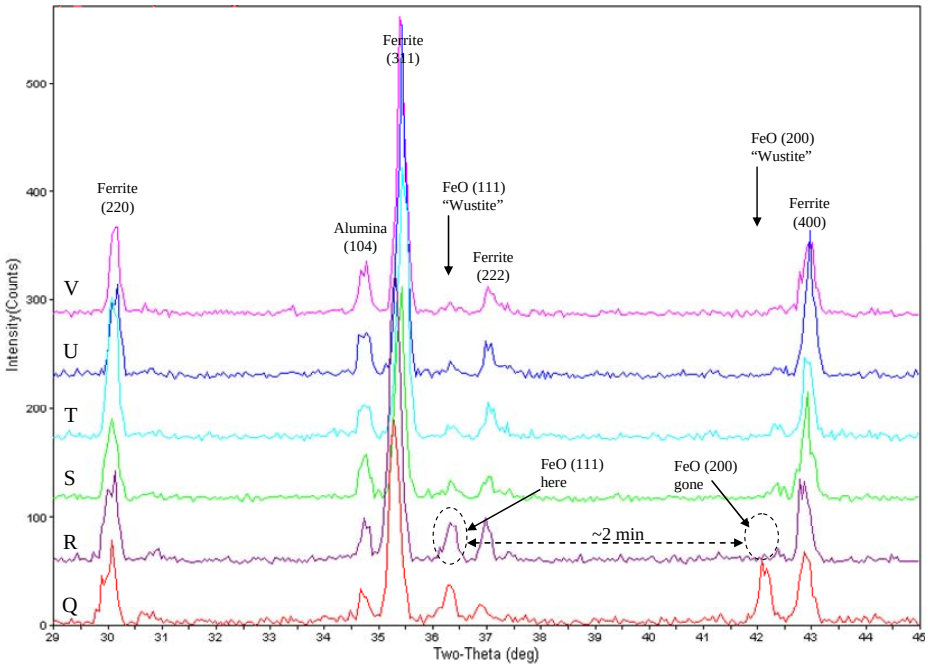

Figure 4. XRD patterns extracted from Figure 3 illustrating fast and slow oxidation processes on switching from He flow (scan Q) to CO_2 flow (scans R – V). All scans were collected at 1100 °C.

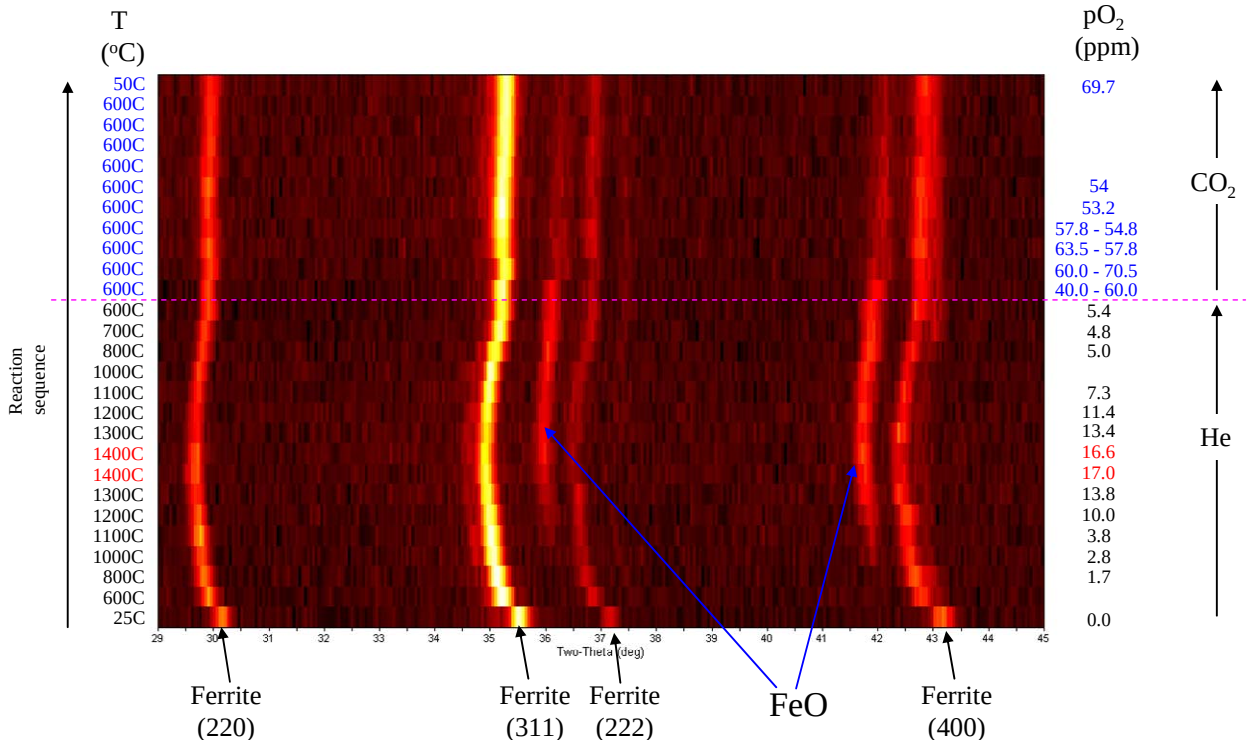

Figure 5. Stacked plot of XRD intensities as function of temperature (left) and environment (right). The indicated O_2 concentration downstream of the sample cell is included. Thermal reduction under He; re-oxidation under CO_2 (at low temperature). For simplicity, cobalt is omitted from the labels.

The ferrite materials recovered from the above experiments were characterized by conventional XRD at room temperature to check phase purity. It was found that the thermally reduced samples which were exposed to air at 1100 °C (and not re-reduced) consisted of ferrite only. Those which were thermally reduced and then exposed to CO_2 at 1100 °C contained a small quantity (~ 1 – 2 %) of Co_xFe_yO (wustite) in addition to the ferrite, as shown in Figure 6. The thermally reduced sample which was re-oxidized by CO_2 at 600 °C (not shown) contained 4 % wustite. Table 1 summarizes the compositions and lattice parameters of the reactive materials shown in Figure 6, as well as the material re-oxidized by CO_2 at 600 °C. Interestingly, the ferrite lattice parameter varied by at most 0.005Å between samples, indicating that while the ferrite undergoes phase separation at high temperature, the sample does not change significantly in composition. Note too, that the ferrite lattice parameter does not vary even when there is significant Co_xFe_yO phase fraction remaining upon cool down. This implies that the reduced phase is similar in Fe:Co ratio to the ferrite and will return to its original ferrite lattice upon re-oxidation.

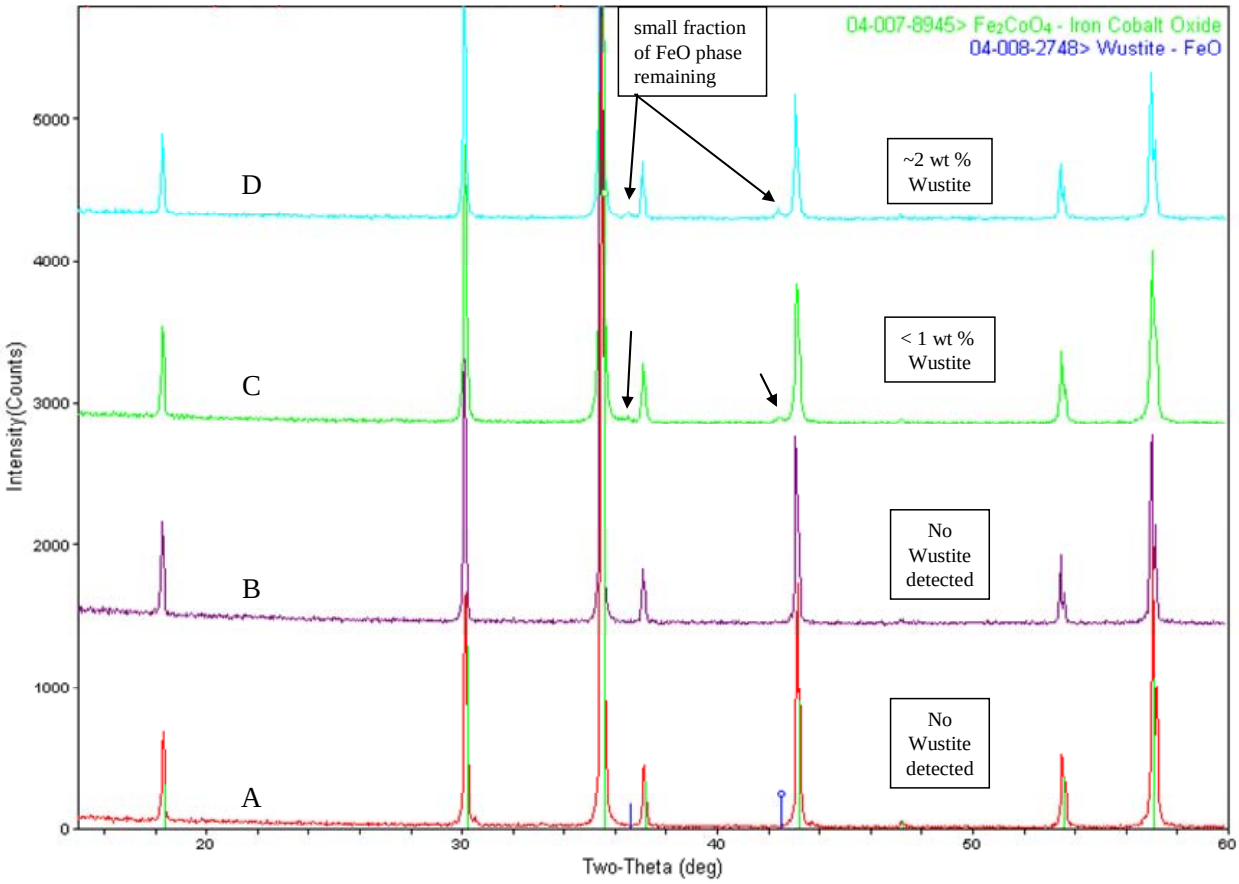

Figure 6. XRD patterns of reactive materials before (A) and after various thermochemical cycles (B – D). Sample B: thermally reduced 1400 °C; re-oxidized in air, 1100 °C. Sample C: thermally reduced 1400 °C; re-oxidized in CO_2 with high O_2-content, 1100 °C. Sample D: thermally reduced 1400 °C; re-oxidized in CO_2 with lower O_2-content, 1100 °C. All scans were collected at room temperature.

A further series of experiments was conducted employing chemical reduction of the ferrite, instead of thermal reduction. These experiments were important to understand the different phases which may be present depending on the reduction method, since the bench reactor tests (described below) relied on chemical reduction to produce the active material for CO_2-splitting.

A sample which was heated to 600 °C under He gas within the XRD reactor chamber, then exposed to forming gas (3% H_2) converted entirely to an FeCo alloy, identified as Wairauite, within 30 minutes. In the initial stages of reduction, a small fraction of wustite (Co_xFe_yO) was detected, as shown in Figure 7. TGA under forming gas (5% H_2) corroborates the in-situ XRD. A sample of $Co_{0.95}Fe_{2.05}O_4$ was heated under the forming gas at a rate of 10 ºC min^{-1} to 800 ºC. A smooth weight reduction, beginning at 504 ºC was seen, implying direct conversion of the spinel to Wairauite without phase separation of the Co- or Fe-oxides. The total weight loss (24.8%) corresponds to complete loss of oxygen in the sample, which was confirmed by XRD of the sample post-TGA. The higher temperature for complete conversion to Wairauite (800 °C) seen in the TGA study compared to the XRD study could be a consequence of the fast heating rate in the TGA experiment; the ~30 minutes taken to heat from 504 °C (onset of

reduction) to 800 °C in the TGA correlates closely with the ~30 minutes for total reduction at 600 °C in the XRD.

Table 1. Phase composition and lattice parameters from XRD after thermochemical cycling.

Sample*	$CoFe_2O_4$ (ferrite) lattice parameter (Å)	$CoFe_2O_4$ wt. fraction (%)	$(Co_xFe_y)O$ lattice Parameter (Å)	$(Co_xFe_y)O$ wt. fraction (%)
A	8.377(2)	100		0
B	8.382(2)	100		0
C	8.378(2)	99		~1
D	8.381(2)	98	4.258	2
E	8.379(2)	96	4.262	4

* See caption to Figure 6 for sample descriptions. Sample E: thermally reduced 1400 °C; re-oxidized in CO_2 with low O_2-content, 600 °C.

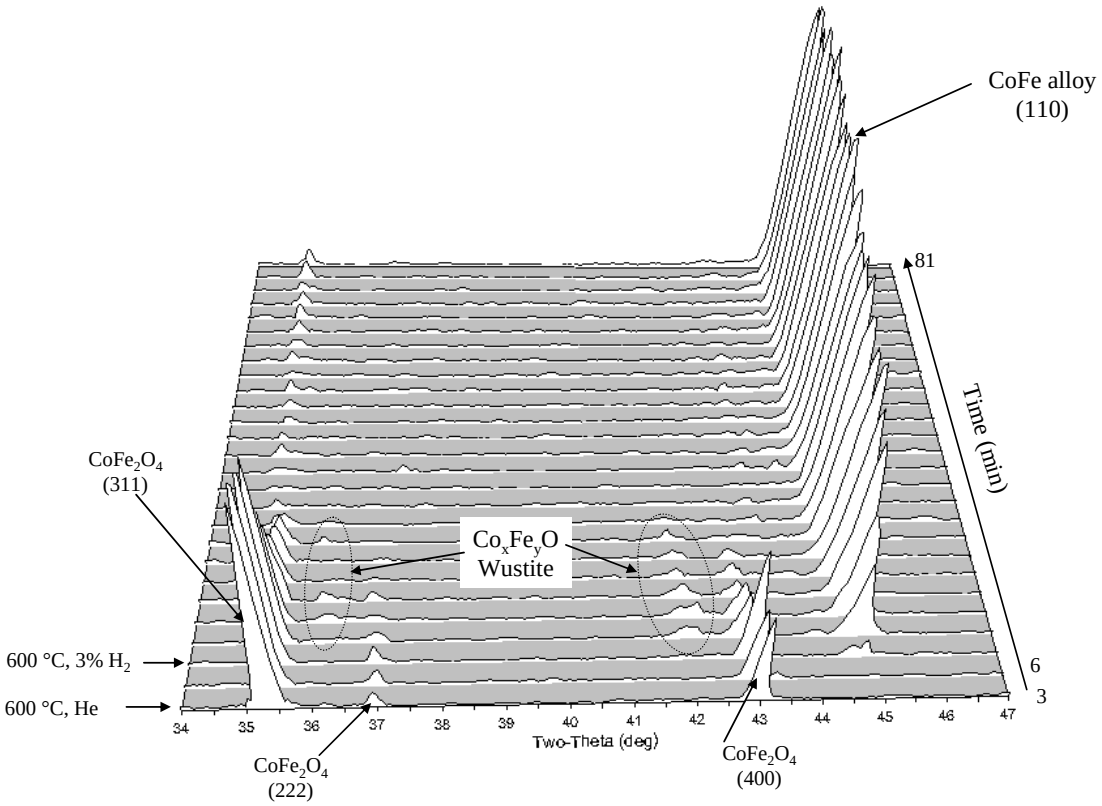

Figure 7a. XRD patterns of reactive materials heated to 600 °C under He (first two patterns) and after exposure to 3% H_2 at 600 °C (remaining patterns).

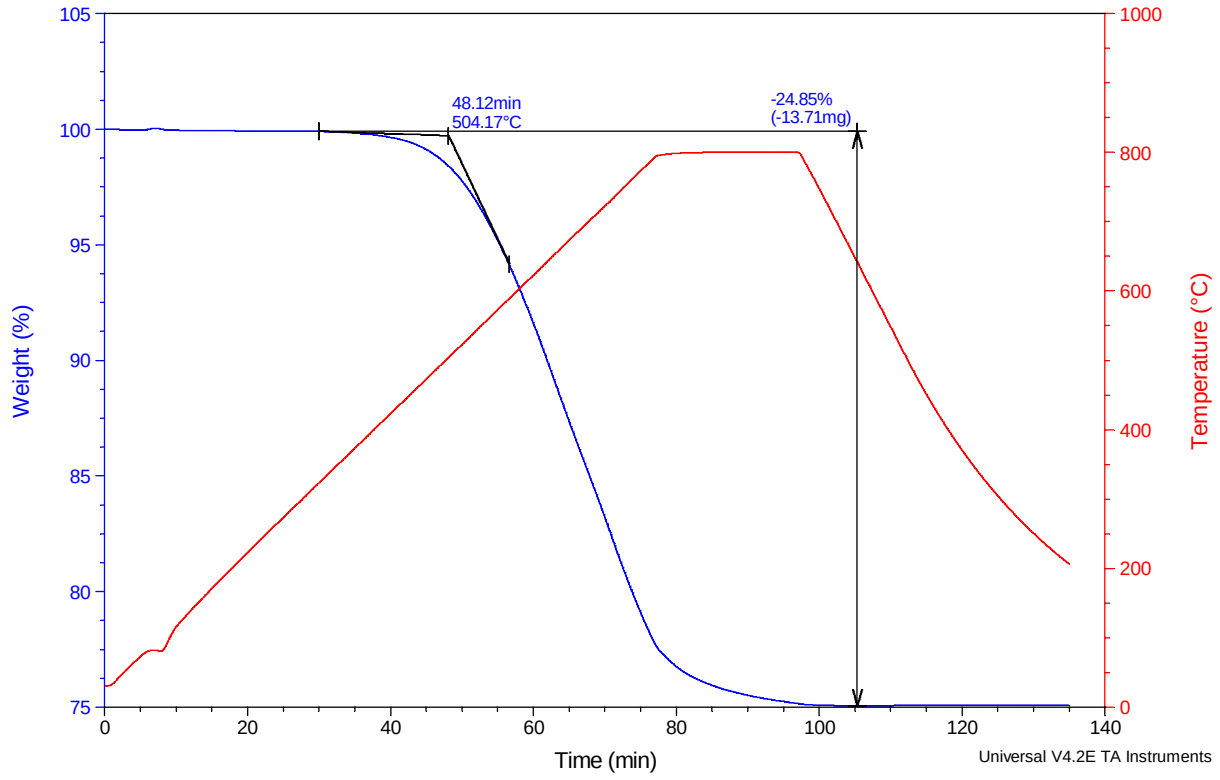

Figure 7b. TGA of $Co_{0.95}Fe_{2.05}O_4$ under forming gas (5% H_2 in Ar) showing conversion to CoFe alloy.

B) Bench reactor evaluation of reactive materials

Initial studies were conducted in order to optimize the reactor configurations and analytical systems for CDS, and to begin scoping operational boundaries for evaluating the performance of ferrite materials in both the tube furnace and TEOM. In addition, some temperature-programmed reductions were performed in the TEOM to understand the chemical reduction process, and on the TGA to begin to elucidate the redox reactions in the ferrite material.

i) Temperature-programmed reduction

As-prepared ferrites ($Co_{0.67}Fe_{2.33}O_4$, supported on ZrO_2 or YSZ, or un-supported) were oxidized by air at 600 °C for 2 hrs in the TEOM, then cooled to 50 °C under nitrogen. Under 5 % H_2/N_2, a temperature ramp from 50 to 700 °C with 30 min soak at 700 °C was initiated, and the mass of the sample was recorded as a function of time (temperature) to generate a temperature-programmed reduction (TPR) curve. Note that the data reported is normalized to the ferrite fraction (i.e., mass of support subtracted out; neglecting any reduction of the support). Two temperature ramp rates were investigated: 2 °C min^{-1} (Figure 8A) and 0.25 °C min^{-1} (Figure 8B). By comparing the data in Figures 8A and 8B, it can be concluded that ferrite/YSZ possesses faster reduction kinetics than ferrite/ZrO_2 (Figure 8A) although the pseudo-equilibrium

data in Figure 8B shows that ferrite/ZrO_2 reduces at a lower temperature than ferrite/YSZ. Reduction of the ferrite/ZrO_2 was complete by 460 °C, while the ferrite/YSZ finished reducing at 520 °C. The un-supported ferrite, however, required a temperature of ~ 650 °C for reduction to be complete. Both supported ferrites achieve a similar overall degree of reduction, while the un-supported material is not able to be reduced to such a deep level under these conditions. It is not clear why the mass loss observed for the un-supported ferrite (~15 %) is less than that found by TGA (Figure 7b).

It should be noted that in-situ XRD (above) identified that the chemically-reduced ferrite was in fact a metallic CoFe alloy. If one assumes the air-oxidized starting material is $Co_{0.67}Fe_{2.33}O_4$, and the material at the end of the TPR run is a CoFe alloy with the same Co:Fe ratio as the ferrite, a mass loss of ~ 27 % would be expected, i.e., close to the experimental mass losses in Figure 8 (as opposed to only 7 % expected mass loss for conversion to wustite).

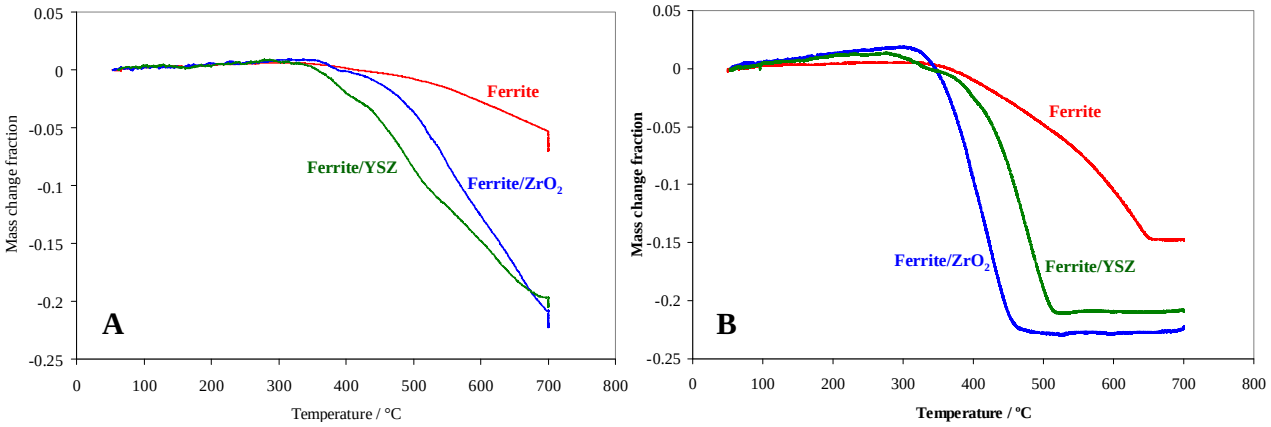

Figure 8. TPR curves of ferrites after oxidation at 600 °C under air. Reduction is measured as a mass loss due to the extraction of oxygen from the ferrite. Reduction under 5 % H_2/N_2 at a ramp rate of 2 °C min^{-1} (A) and 0.25 °C min^{-1} (B), followed by 30 minute hold at 700 °C. Mass data are normalized to the ferrite fraction in the mixture.

ii) Isothermal reactions.

These experiments were conducted in a tube furnace with high thermal inertia, thus any changes in set temperature were allowed at least 1 hour to stabilize. Note also that these experiments were conducted under conditions of very low flow rate (i.e., long contact time), typically ~ 6 ml min^{-1}, in order to achieve non-negligible conversions since at the low temperatures used the kinetics of CDS are slow.

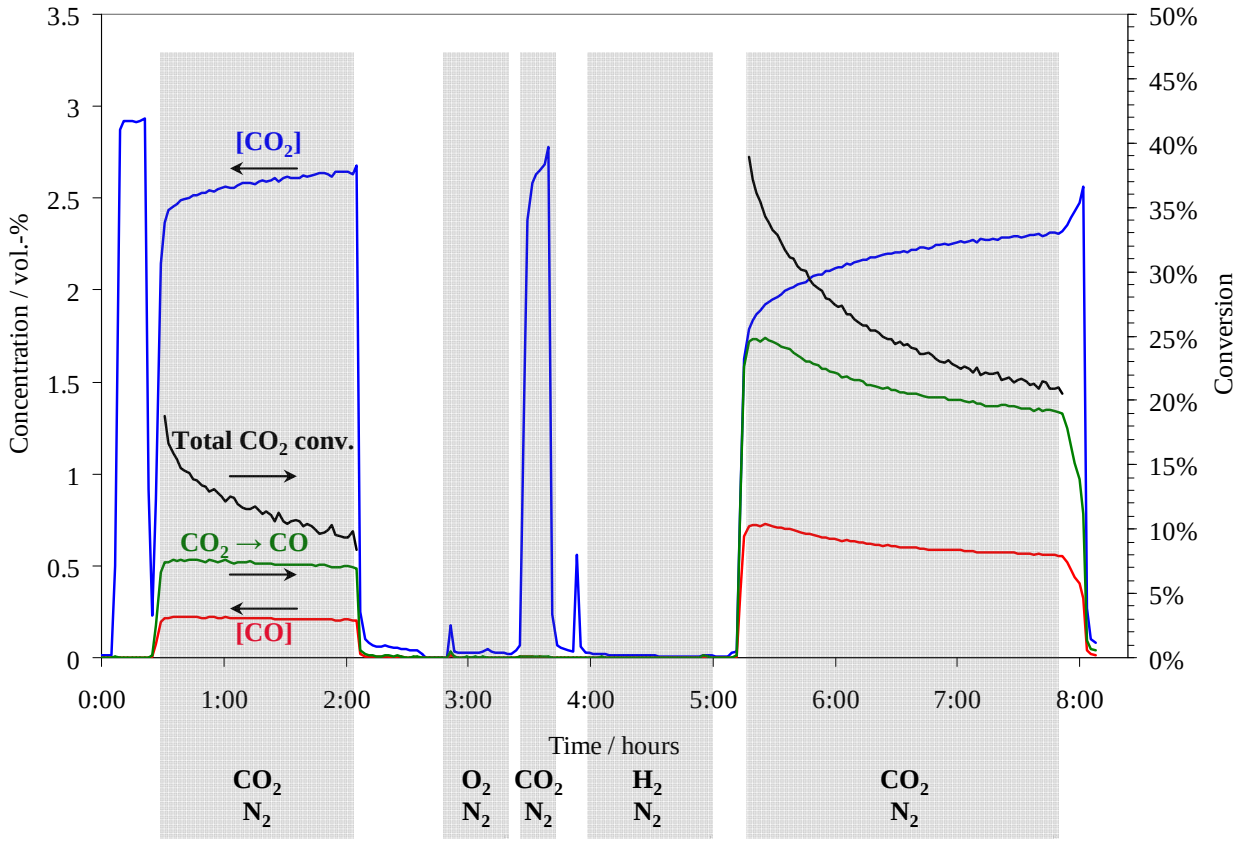

Figure 9. Bench reactor evaluation of un-supported $Co_{0.67}Fe_{2.33}O_4$ at 600 °C. For the first 30 minutes the reactor was bypassed to verify the composition of the feed gas (nominal 3% CO_2 in N_2). Shaded areas represent period of exposure to gases indicated at bottom; un-shaded areas = inert purge. Space velocity during CDS = 2100 ml_{gas} $ml_{ferrite}^{-1}$ $hour^{-1}$.

The results shown in Figure 9 were recorded after several preliminary scoping tests were made to verify the reactor and analytical system were working satisfactorily, and the un-supported ferrite had been operated for several days under a variety of conditions (both reductive and oxidative). Around 7% conversion of CO_2 to CO was recorded in the first 2 hrs of the experiment at 600 °C. The cause of the mismatch between CO_2-to-CO and total CO_2 conversions at early times is not clear. One possibility is that certain active sites in the ferrite are decomposing CO_2 to carbon; however this is not supported by the meager quantity of CO_2 emitted during subsequent re-oxidation of the material (around 3 hrs into the experiment). After re-oxidation, the ferrite was again exposed to 3% CO_2 in order to verify that the oxidized material was inactive for CDS; indeed, no CO was detected. The ferrite was then chemically reduced for one hour before re-starting the CO_2-splitting reaction. The conversion of CO_2 to CO was then approximately three times higher than at the beginning of the experiment, and was approaching steady state operation after about 2 ½ hours reaction. This experiment showed that a) the material does not split CO_2 when it is in its oxidized form; b) large differences in CO_2 conversion can be expected depending on the sample's history; and c) a discrepancy between the apparent total CO_2 conversion and CO_2-to-CO conversion exists after beginning the splitting reaction, which is not due to coking of the ferrite but is probably an artifact of the experimental setup. An estimation of the moles CO_2 emitted during re-oxidation gave a figure at least one

order of magnitude lower than the quantity constituting the difference between the integrated "total CO_2 conversion" and the integrated "CO_2-to-CO conversion."

Figure 10 illustrates the effect of temperature on the CDS reaction. This experiment was conducted after that shown in Figure 9, with no regeneration. The reactor was simply purged with N_2 and cooled to ambient temperature between the two experiments. The CO_2 conversion at the beginning of Figure 10, and the end of Figure 9 are within 1% of each other, indicating good reproducibility. Each 50 °C temperature increase resulted in a boost in initial CO_2 conversion. While steady state conversion of CO_2 to CO was achieved within 1 hr at 600 °C, at higher temperatures steadily declining conversions were recorded. On returning to 600 °C at the end of the experiment, the performance for the CO_2-splitting reaction had declined significantly compared to the beginning of the experiment. Integrating the total CO evolved from the CDS reaction since the last regeneration (in previous experiment, Figure 9) to the end of the experiment in Figure 10, and equating each CO molecule evolved to one oxygen atom re-absorbed by the reduced ferrite, one concludes that approximately 40% of the ferrite has been re-formed at the end of Figure 10. This may explain the apparent deactivation in Figure 10, since at higher levels of re-oxidation oxygen has further to diffuse through the ferrite matrix to reach wustite. This is assuming that the reaction front progresses from the shell of a reduced ferrite particle towards the core.

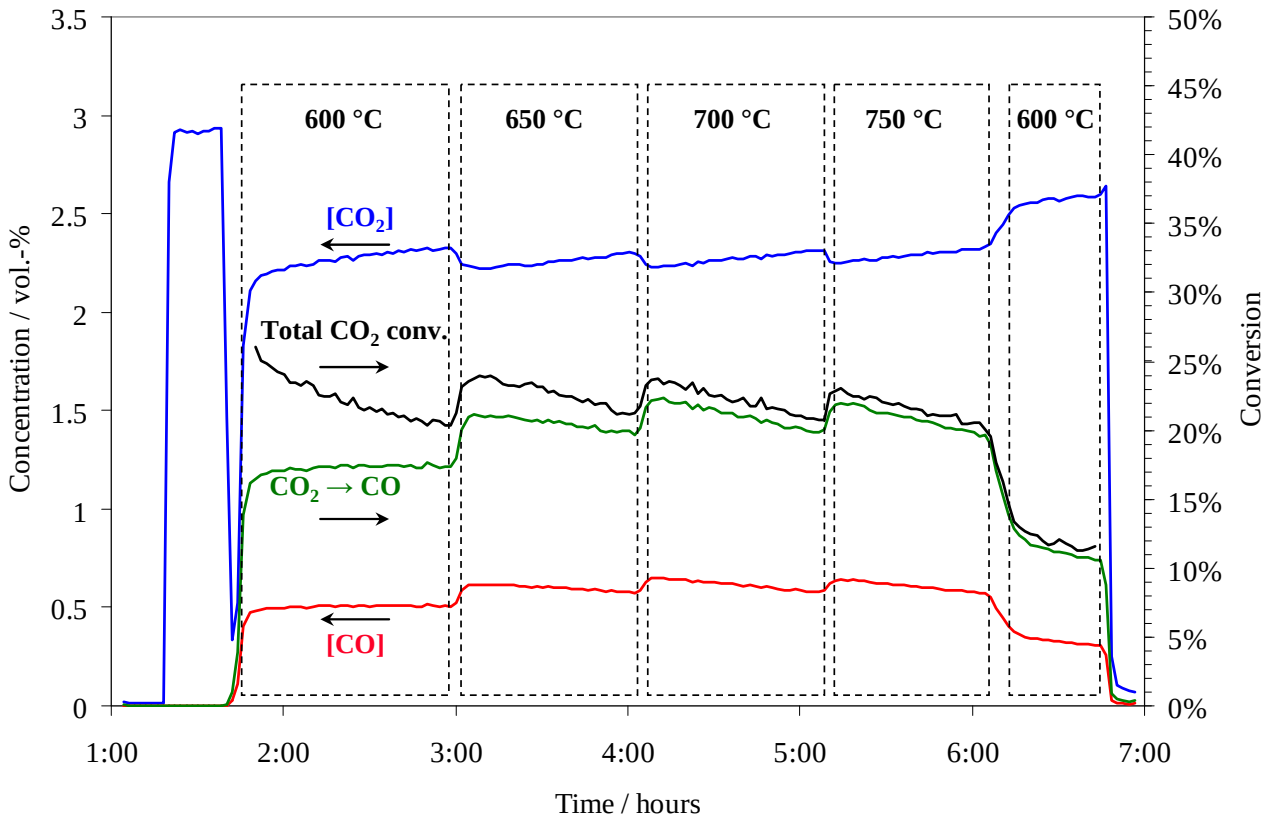

Figure 10. Bench reactor evaluation of un-supported $Co_{0.67}Fe_{2.33}O_4$ at 600 – 750 °C under 3% CO_2. For first 45 minutes reactor was bypassed to verify composition of feed gas (nominal 3% CO_2 in N_2). Space velocity = 2100 ml_{gas} $ml_{ferrite}^{-1}$ $hour^{-1}$.

iii) Redox-cycling experiments

Examples of reduction–oxidation cycling experiments in the TEOM for $Co_{0.67}Fe_{2.33}O_4$ supported on ZrO_2 and YSZ are given in Figure 11. In these experiments, the reduction temperature (T_R) was 400 °C, and the re-oxidation temperature (T_{OX}) was 600 °C. Prior to beginning the CDS experiment, the ferrite was reduced under 5% H_2 at 600 °C for 5 hrs. The saw-tooth appearance was caused by the individual temperature cycles (inset; changes in buoyancy with temperature give a false mass increase during up-ramp and mass decrease during down-ramp), while the gradual increase in mass over the course of the experiment was due to the net slow re-oxidation of the mixed-metal oxide. The ferrite/YSZ re-oxidized slightly faster than the ferrite/ZrO_2, and neither material reached steady-state in the 2100 min experiment.

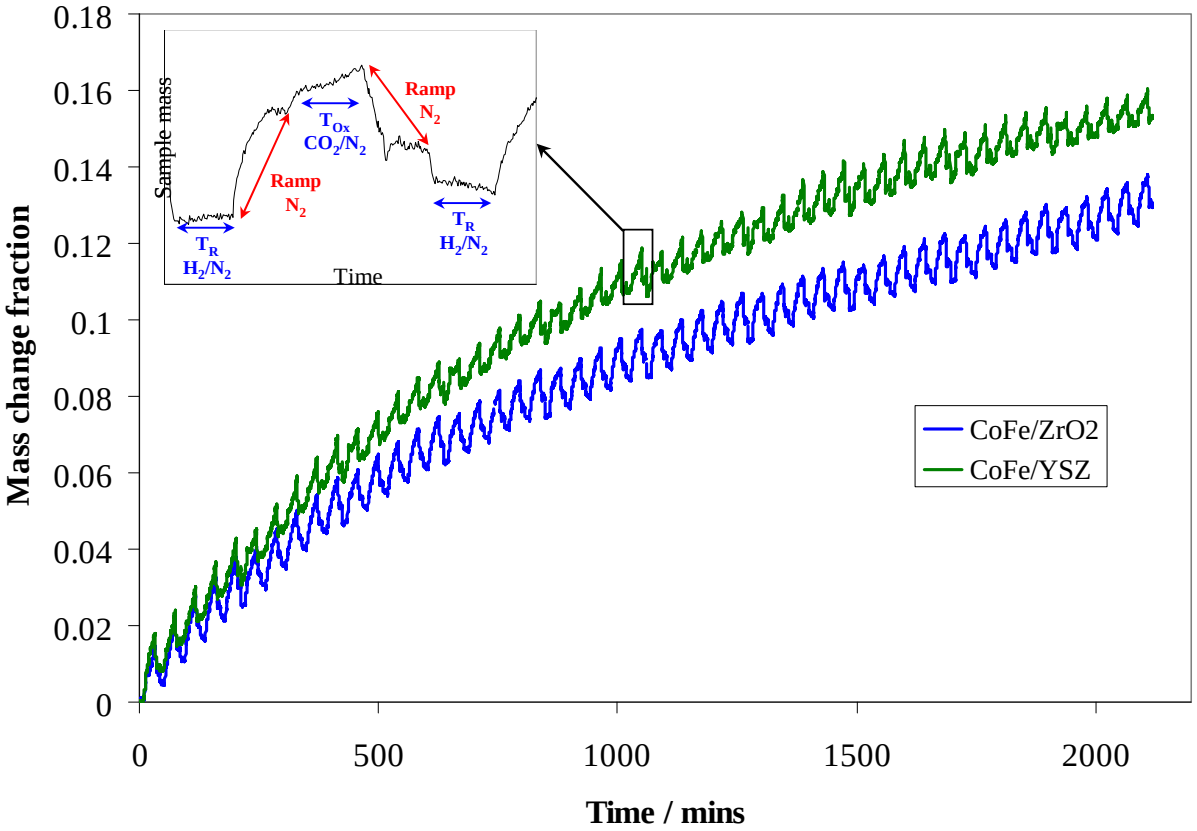

Figure 11. TEOM evaluation of $Co_{0.67}Fe_{2.33}O_4$ supported on ZrO_2 and YSZ during temperature/redox cycling. Reduction temperature (T_R) = 400 °C, re-oxidation temperature (T_{OX}) = 600 °C. Each step in cycle (see inset) ~ 10 minutes. Mass data are normalized to the ferrite fraction in the mixture.

A series of experiments where T_R and T_{OX} were varied in 100 °C increments lead to the general conclusions that YSZ-supported mixed metal oxides reduce and re-oxidize faster than ZrO_2-supported ones, and larger temperature swings between reducing and oxidizing conditions result in higher levels of re-oxidation over the course of the experiment. The faster kinetics of reduction and oxidation of the YSZ-supported metal oxides may be attributed to enhanced oxygen transport through the YSZ lattice compared to the ZrO_2 lattice. All experiments where $T_{OX} > T_R$ showed a similar profile to that in Figure 11, whereas experiments where $T_{OX} = T_R$

showed an overall drop in mass with time. This latter observation indicates that the rate of chemical reduction of ferrite is faster than the rate of re-oxidation via CDS, at least in the temperature range 400 – 700 °C.

Similar to the observations from the TPR experiments, the change in sample mass on oxidation was higher than that expected for wustite (reduced form) to ferrite (oxidized form) transition, since the chemically reduced starting point was a metallic CoFe alloy, not wustite.

iv) Thermogravimetric analysis (TGA)

TGA was performed on $Co_{0.95}Fe_{2.05}O_4$ samples under simulated WS and CDS conditions (Figure 12). The samples were heated to 1400 °C under Ar gas at a rate of 20 °C min^{-1}, held isothermally for approximately 2 hrs, cooled to 1100 °C, and exposed to either water vapor (approximately 34% RH) in Ar or CO_2 (19.95% in Ar balance) over 2 hrs. The concentrations (ppm) of CO_2 and water vapor in the Ar were calculated to be similar to one another.

Both experiments show the expected reduction under Ar at 1400 ºC, though it is worth noting that the kinetics are quite slow. Even after 2 hrs, the samples have not reduced completely. The oxidation reaction is much faster. The oxidation by CO_2 occurs almost instantaneously, while that by H_2O is slower. However, this may be due in part to the assumption that it takes inherently longer for the system to come to equilibrium when switching to water vapor than it does when switching from Ar to Ar/CO_2. The magnitude of oxidation via CO_2 is also larger than that by H_2O. XRD of the samples post-TGA showed no presence of wustite, unlike those of the in-situ XRD oxidized CO_2 at 1100 ºC. The most likely reason for this may lie in the longer oxidation times and slower temperature ramps during the TGA experiments, which may have allowed a more complete conversion back to the ferrite spinel.

v) Future direction for bench reactor tests

Future bench tests will employ a dedicated high temperature tube furnace capable of operation to 1700 °C. Such a furnace was purchased towards the end of this project, and is available for Sandia's ongoing efforts in thermochemical conversions. This furnace will allow in-situ thermal reduction instead of chemical reduction, thus avoiding the complication of over-reduction to metallic alloy, as observed by XRD. In addition, the new furnace will allow CDS and WS reactions to be performed at higher temperature where the kinetics of reactions (2) and (3) are improved.

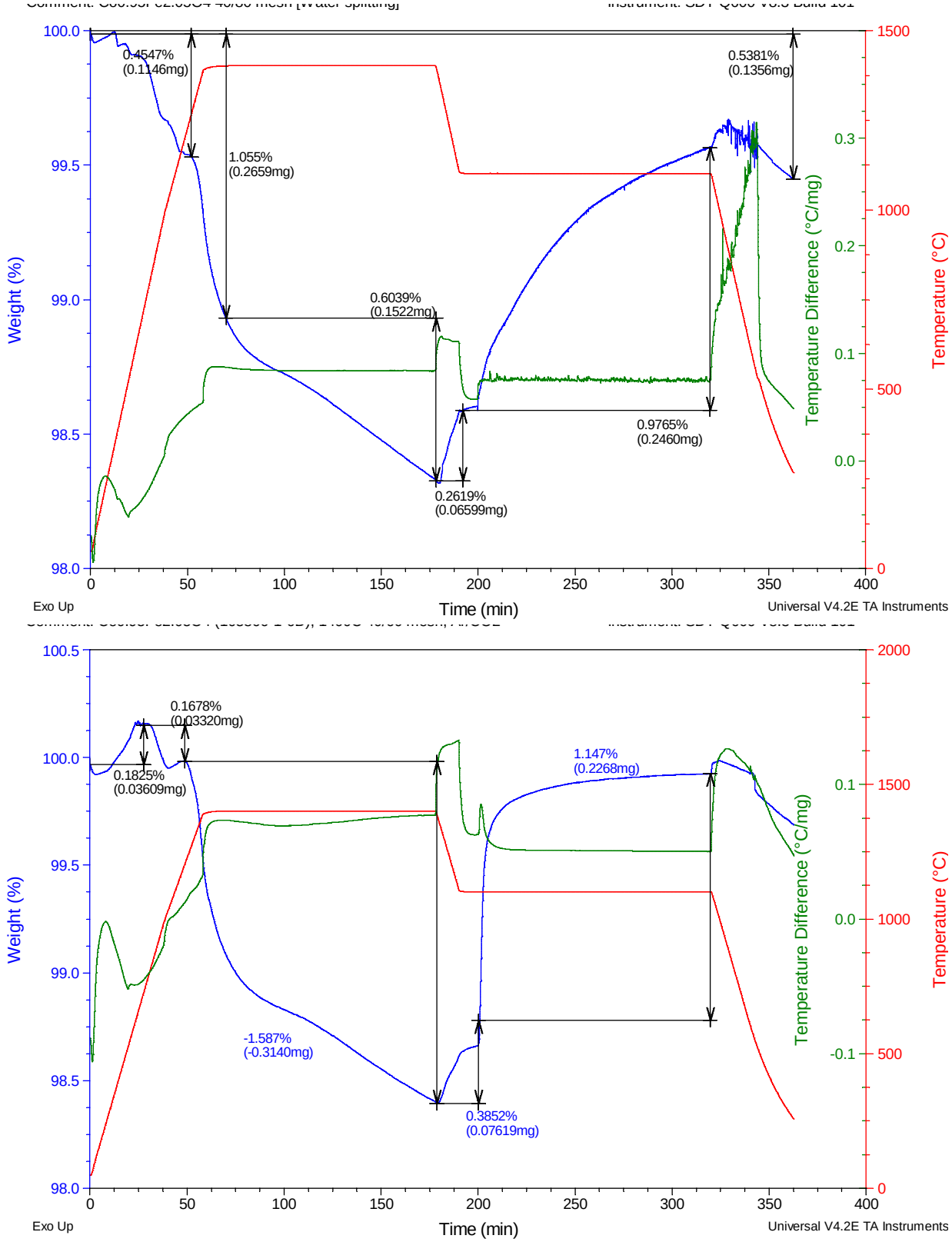

Figure 12: TGA of $Co_{0.95}Fe_{2.05}O_4$ under reduction conditions and simulated WS (top) and CDS (bottom) reactions.

C) Water splitting thermodynamics

This effort was lead at Northwestern University by Prof. Chris Wolverton.

In this work, the temperature and pressure regimes in which the TR and WS steps of the cycle are thermodynamically favorable in terms of the enthalpy and entropy of oxide reduction, were determined. These metrics represent a useful design goal for any proposed WS cycle. Applying this theoretical framework to available thermodynamic data, it was shown that none of the 105 binary oxide redox couples that were screened possess both energetically favorable reduction and oxidation steps. However, several driving forces, including low pressure and a large positive solid-state entropy of reduction of the oxide, have the potential to enable thermodynamically-favored two-step cycles. The results of this work are summarized in a draft publication attached to this report as Appendix A: "General thermodynamic analysis of two-step thermochemical water-splitting cycles."

SUMMARY

Cobalt ferrites were synthesized by a simple co-precipitation method, and were optionally supported on ZrO_2 or YSZ. In-situ XRD verified that the ferrite phase reduced partially to wustite (Co_xFe_yO, where $x + y = 1$) on heating to 1400 °C under helium. Subsequent exposure to air at 1100 °C caused immediate re-oxidation, and reheating to 1400 °C in He re-formed the wustite phase. If the wustite phase was exposed to CO_2 at 1100 °C, a gradual re-oxidation of wustite to ferrite occurred, however background oxygen levels had to be minimized to prevent rapid re-oxidation. Chemical reduction of the ferrite produced a metallic CoFe alloy, however bench reactor tests using chemical reduction showed that the alloy was also active for CDS. Temperature- and redox-cycling tests in a TEOM revealed that a ferrite/YSZ material possessed overall faster kinetics for oxidation/reduction than a ferrite/ZrO_2 material, presumably due to enhanced oxygen transport through the YSZ phase. Temperature programmed reduction verified that the ferrite/YSZ reduced at a lower temperature than ferrite/ZrO_2 when using a ramp rate of 2 °C min^{-1}. However, when a slower ramp rate was used (0.25 °C min^{-1}; a "pseudo-equilibrium" experiment), the zirconia-supported material reduced at a lower temperature than the YSZ-supported one.

Thermodynamic modeling revealed that the quantities $\Delta H_{reduction}$ and $\Delta S_{reduction}$, which represent the enthalpy and entropy differences between reduced and non-reduced materials participating in thermolysis, together determine the thermodynamic performance of WS cycles based on those materials. In the absence of $\Delta S_{reduction}$, only a very large ΔT (>1000K) between the TR and WS steps would give both steps negative Gibbs free energies of reaction. In most binary oxide redox reactions, $\Delta S_{reduction}$ is negative, and further penalizes the water splitting cycle's thermodynamics. However, it is important to note that a material with a very large $\Delta S_{reduction}$ could, if it also had an appropriate $\Delta H_{reduction}$, operate with favorable TR and WS thermodynamics and potentially represent a dramatic improvement over present WS materials. It was also observed that any thermolysis cycle, whether or not both steps are favorable, can benefit from reduced TR pressure and non-equilibrium techniques such as sweep gases.

Finally, it is hypothesized that a cycle with one unfavorable step (the vast majority, at least of the binary oxides) ought to favor WS over TR, since WS is more likely to be kinetically hindered; many of the most widely investigated WS materials today follow this prescription.

REFERENCES

(1) Steinfeld, A. *Solar En.* **2005**, *78*, 603.
(2) Kodama, T. *Prog. En. Comb. Sci.* **2003**, *29*, 567.
(3) Nakamura, T. *Solar En.* **1977**, *19*, 467.
(4) Kodama, T.; Nakamuro, Y.; Mizuno, T. *J. Solar En. Eng.* **2006**, *128*, 3.
(5) Kodama, T. et al., *Proceedings of the ASME ISES Conference*, Hawaii, **2003**.
(6) Miller, J.E.; Allendorf, M.D.; Diver, R.B.; Evans, L.R.; Siegel, N.P.; Stuecker, J.N., *J. Mater. Sci*. **2008**, *43*, 4714–28.
(7) Ehrensberger, K.; Frei, A.; Kuhn, P.; Oswald, H. R.; Hug, P. *Sol. St. Ionics* **1995**, *78*, 151.
(8) Kodama, T.; Kondoh, Y.; Yamamoto, R.; Andou, H.; Satou, N. *Solar En.* **2005**, *78*, 623.
(9) Ishihara, H.; Kaneko, H.; Yokoyama, T.; Fuse, A.; Hasegawa, N.; Tamaura, Y. *Proceedings of ISEC 2005 International Solar Energy Conference*, Orlando, FL, ISEC2005-76151.
(10) Aoki, H.; Kaneko, H.; Hasegawa, N.; Ishihara, H.; Takahashi, Y.; Suzuki, A.; Tamaura, Y. ISEC 2004, 2004, Portland, OR, ISEC2004-65068.
(11) Tamaura, Y.; Kojima, N.; Hasegawa, N.; Inoue, M.; Uehara, R.; Gokon, N.; Kaneko, H. *Int. J. Hydrogen En.* **2001**, *26*, 917.
(12) Tamaura, Y.; Kaneko, H. *Solar En.* **2005**, *78*, 616.
(13) Kodama, T.; Gokon, N. *Chem. Rev.* **2007**, *107*, 4048.
(14) Diver, R.B; Miller, J.E.; Allendorf, M.D.; Siegel, N.P.; Hogan, R.E. *Proceedings of ISEC 2006 International Solar Energy Conference*, Denver, CO, ISEC2006-99147
(15) Miller, J.E. *SAND Report*, SAND2007-8012 **2007**.

APPENDIX A: "GENERAL THERMODYNAMIC ANALYSIS OF TWO-STEP THERMOCHEMICAL WATER-SPLITTING CYCLES"

There follows a draft publication originating from Northwestern University. The work described in the publication was funded under this project.

General Thermodynamic Analysis of Two-Step Thermochemical Water-Splitting Cycles

B. Meredig and C. Wolverton

Department of Materials Science and Engineering,

Northwestern University, Evanston, IL 60208

We present an analysis of the equilibrium thermodynamics of a two-step metal oxide water splitting cycle. Our straightforward treatment of redox-based water splitting chemistry is powerful and unique in that it is completely general, so that the conclusions herein hold for *all materials* used for such a process. We determine the temperature and pressure regimes in which the thermal reduction (TR) and water oxidation (WO) steps of the cycle are thermodynamically favorable in terms of the enthalpy and entropy of oxide reduction, which represents a useful design goal for any proposed water splitting cycle. Applying this theoretical framework to available thermodynamic data, we show that none of the 105 binary oxide redox couples we screened will have both energetically favorable reduction and oxidation steps. However, several driving forces, including low pressure and a large positive solid-state entropy of reduction of the oxide, have the potential to enable thermodynamically-favored two-step cycles.

Keywords: thermochemical water splitting, thermolysis, redox, metal oxide, cycle, thermodynamics

I. Introduction

Water thermolysis is a promising means to produce hydrogen by thermochemically splitting water molecules. Directly splitting H_2O with thermal energy requires impractical temperatures of about 4300K,[1] as well as a gas separation mechanism,[2,3] so recent work has generally focused on identifying materials that can reversibly participate in a lower-temperature redox cycle whose net output is $H_2+½O_2$. This redox cycle can, in principle, have an arbitrary number of steps; the larger the number of steps, the lower the temperatures needed for each, but the lower the cycle's maximum thermodynamic efficiency.[4] Thus, two-step (or, in some instances, three-step[5]) cycles seem to represent the best combination of feasible reaction temperatures and thermodynamic efficiency. In a typical two-step thermolysis cycle, the subject of this work, an oxide material is reduced at very high temperature (up to 2000K). Then, the material re-oxidizes by reacting with water vapor and generating hydrogen gas (at around 1000K). These materials generally are metal oxides, and the two reaction steps can be represented as:

$$MO_x \rightarrow MO_{x-1} + \frac{1}{2}O_2 \text{ and} \quad (1)$$

$$MO_{x-1} + H_2O \rightarrow MO_x + H_2, \quad (2)$$

where M is a metal, MO_x is the corresponding metal oxide, and MO_{x-1} is the reduced oxide. Reaction (1) is called the thermal reduction (TR) step, and reaction (2) is the water oxidation (WO) step. Although reactions (1) and (2) are written schematically in terms of simple binary, stoichiometric line compounds, they can represent much more complex situations as well, e.g., off-stoichiometric phases, solution phases, and multi-component oxide materials. For instance, M might generally represent a combination of metals, and MO_{x-1} the reduced oxide products, which could be a mixture of an arbitrary

number of compounds or solution phases. In a simple case, MO_x might represent $2CeO_2$ and MO_{x-1} would represent Ce_2O_3. In a more complex case, where MO_x is $3CoFe_2O_4$ and a two-step decomposition takes place,[6] MO_{x-1} would be ($2Fe_3O_4$ + 3CoO) for the first stage; MO_x then becomes Fe_3O_4 and MO_{x-1} 3FeO for the second stage. We return to the issue of off-stoichiometric and solution phases below.

The purpose of this analysis is to understand the factors entering the thermodynamics of a *general* two-step thermolysis cycle. There are many previous discussions of the thermodynamics of particular water splitting cycles available in the literature, in the form of new cycle proposals,[2,7-9] materials-specific analyses,[10-14] and reviews.[1,4,15-19] Of particular note is Abanades *et al.*'s analysis of 280 proposed water-splitting methods, some of which are quite exotic, based on thermodynamics as well as other factors.[5] However, these studies all focus on the thermodynamic functions of *specific* metal redox couples; in contrast, we are interested in elucidating the generic driving forces which contribute to a thermodynamically preferred two-step cycle. We seek to establish quantitative regimes for operating temperatures and pressures, as well as the enthalpy and entropy differences between MO_x and MO_{x-1}, that provide favorable thermodynamics for water thermolysis. Using thermodynamic databases, we apply the results of our analysis to 105 binary redox reactions; surprisingly, none of these candidates operates near this window of favorable *equilibrium* thermodynamics. Several of these materials are presently used in water-splitting processes, indicating that nonequilibrium and kinetics considerations are especially important in enabling the reactions to occur. We further show that the entropy difference between MO_x and MO_{x-1} is non-negligible even compared to the gaseous species in the reactions, and can in combination with the solid-state enthalpy difference potentially drive water-splitting. We characterize this ΔH-ΔS relationship and use it to quantitatively delineate a window in which both TR and WO are favorable, thus providing a clear design goal for future thermolysis materials.

II. Results and Discussion

A. Temperature Ranges Favorable for Both TR and WO

Ideally, one would like both the TR and WO reactions to be thermodynamically favorable, with negative Gibbs free energies of reaction. Because the steps run at different temperatures, that criterion can be met in certain T_{TR} and T_{WO} ranges, where T_{TR} is the TR step temperature and T_{WO} is the WO temperature. This observation has been made in previous materials-specific analyses (e.g., Kodama and Gokon's review[15]), but here, we examine the thermodynamics for a general two-step cycle. Of course, there are practical physical limits on the temperature extremes: materials degradation and volatility at extremely high temperature and hampered kinetics at low temperature. To find the temperatures associated with favorable energetics, the equilibrium thermodynamic expressions

$$\Delta G_{TR,T_{TR}} = \Delta H_{TR,T_{TR}} - T_{TR} \cdot \Delta S_{TR,T_{TR}} \leq 0 \text{ and} \tag{3}$$

$$\Delta G_{WO,T_{WO}} = \Delta H_{WO,T_{WO}} - T_{WO} \cdot \Delta S_{WO,T_{WO}} \leq 0 \tag{4}$$

must be satisfied. The notation we adopt here and maintain throughout is that a *TR* or *WO* subscript indicates which of the two steps is under consideration, while a T_{TR} or T_{WO} subscript specifies the temperature at which each thermodynamic quantity is computed. The enthalpies and entropies in Eqs. 3 and 4 can be expressed in terms of those of the chemical reactants and products in Eqs. 1 and 2, so that

$$\Delta H_{TR,T_{TR}} = H_{T_{TR}}^{MO_{x-1}} + \frac{1}{2} H_{T_{TR}}^{O_2} - H_{T_{TR}}^{MO_x}, \tag{5}$$

$$\Delta S_{TR,T_{TR}} = S_{T_{TR}}^{MO_{x-1}} + \frac{1}{2} S_{T_{TR}}^{O_2} - S_{T_{TR}}^{MO_x}, \tag{6}$$

$$\Delta H_{WO,T_{WO}} = H_{T_{WO}}^{MO_x} + H_{T_{WO}}^{H_2} - H_{T_{WO}}^{MO_{x-1}} - H_{T_{WO}}^{H_2O}, \text{ and} \tag{7}$$

$$\Delta S_{WO,T_{WO}} = S_{T_{WO}}^{MO_x} + S_{T_{WO}}^{H_2} - S_{T_{WO}}^{MO_{x-1}} - S_{T_{WO}}^{H_2O}. \tag{8}$$

In these equations, the superscript indicates the species associated with each thermodynamic variable. We rewrite these expressions in terms of the *formation* enthalpies, defined as

$\Delta H_f(MO_n) = H(MO_n) - \frac{n}{2}H(O_2) - H(M)$, and standard entropies of the compounds; Eqs. 3 and 4 become

$$\Delta G_{TR,T_{TR}} = \Delta H_{f,T_{TR}}^{MO_{x-1}} - \Delta H_{f,T_{TR}}^{MO_x} - T_{TR}\left[S_{T_{TR}}^{MO_{x-1}} + \frac{1}{2}S_{T_{TR}}^{O_2} - S_{T_{TR}}^{MO_x}\right] \le 0 \quad \text{and} \tag{9}$$

$$\Delta G_{WO,T_{WO}} = \Delta H_{f,T_{WO}}^{MO_x} - \Delta H_{f,T_{WO}}^{MO_{x-1}} - \Delta H_{f,T_{WO}}^{H_2O} - T_{WO}\left[S_{T_{WO}}^{MO_x} + S_{T_{WO}}^{H_2} - S_{T_{WO}}^{MO_{x-1}} - S_{T_{WO}}^{H_2O}\right] \le 0. \tag{10}$$

In these relations, T_{TR} and T_{WO} are chosen reaction temperatures, and any properties relating to MO_x and MO_{x-1} are variables that depend upon the materials used. The other materials-independent quantities are well-characterized experimentally.[20] We next analyze the above expressions, first neglecting the solid-state entropies in the above expression, and then including them.

B. Neglecting Solid-State Entropy

Both the enthalpies and entropies of the oxide species appear in Eqs. 9 and 10, but to simplify the analysis, it would be convenient to eliminate the solids' entropies. Thus, the approximation

$$S^{MO_x} - S^{MO_{x-1}} \approx 0 \tag{11}$$

will be used for now (and later relaxed). That is, the difference in solid-state entropies between the oxide and its reduced form is assumed to be small, especially as compared to the gaseous species in the TR and WO reactions. The notational substitution

$$\Delta H_f^{MO_{x-1}} - \Delta H_f^{MO_x} \equiv \Delta H_{reduction} \tag{12}$$

will also prove useful, since this quantity (assumed temperature-independent) appears in both Eqs. 9 and 10. Applying Eqs. 11 and 12 leaves

$$\Delta G_{TR,T_{TR}} = \Delta H_{reduction} - T_{TR} \cdot \frac{1}{2}S_{T_{TR}}^{O_2} \le 0 \text{ and} \tag{13}$$

$$\Delta G_{WO,T_{WO}} = -\Delta H_{reduction} - \Delta H_{f,T_{WO}}^{H_2O} - T_{WO}\left[S_{T_{WO}}^{H_2} - S_{T_{WO}}^{H_2O}\right] \le 0. \tag{14}$$

Of interest are the TR and WO temperature ranges in which both steps have negative Gibbs free energies of reaction. Setting Eqs. 13 and 14 equal to zero will give the boundary between the thermodynamically favorable and unfavorable regions; then, adding the two equations cancels out the only materials-dependent property ($\Delta H_{reduction}$) and leads to a new expression that depends only on T_{TR} and T_{WO}:

$$0 = T_{TR} \cdot \frac{1}{2} S_{T_{TR}}^{O_2} + \Delta H_{f,T_{WO}}^{H_2O} + T_{WO}\left[S_{T_{WO}}^{H_2} - S_{T_{WO}}^{H_2O} \right]. \quad (15)$$

Defining $\Delta T = T_{TR} - T_{WO}$ and using the definition of the Gibbs free energy of formation of H_2O, we can rewrite Eq. 15 as

$$\Delta T = \frac{-2\Delta G_{f,T_{WO}}^{H_2O} - T_{WO}}{S_{T_{TR}}^{O_2}} \approx \frac{-2\Delta G_{f,T_{WO}}^{H_2O}}{S_{T_{TR}}^{O_2}} \Rightarrow \Delta T \cdot S_{T_{TR}}^{O_2} \approx -2\Delta G_{f,T_{WO}}^{H_2O}, \quad (16)$$

where ΔS is the increase in entropy of O_2 upon heating from T_{WO} to T_{TR}. The ΔS term represents a 6% fraction of the numerator for TR at 2000K and WO at 1000K, and can be neglected in a rough approximation. Eq. 16 gives the value of ΔT for which there is exactly zero thermodynamic driving force for both reactions; wider TR-WO temperature differences are required to have thermodynamically favored reactions. We note the following regarding Eq. 16: First, *there are no materials-dependent properties in the expression*. Thus, the size of the temperature difference between TR and WO reactions is largely independent of material choice, neglecting solid-state entropy. The lack of materials-dependent properties also makes extension of Eq. 16 to reduction of other gases (e.g., CO_2) quite trivial. Second, the criteria for favorable TR and WO are apparent: ΔT and the entropy of O_2 serve as driving forces whose product must equal or exceed twice the free energy of formation of H_2O, which is the barrier to a thermodynamically-preferred two-step cycle. Given that the entropy of O_2 increases with temperature, we would expect the ΔT temperature window should decrease in size for increasing temperature (or, conversely, ΔT should widen as the temperature is lowered). Also, the window ΔT shrinks to zero at the point where $\Delta G_f(H_2O)=0$, corresponding to the direct, one-step

Figures

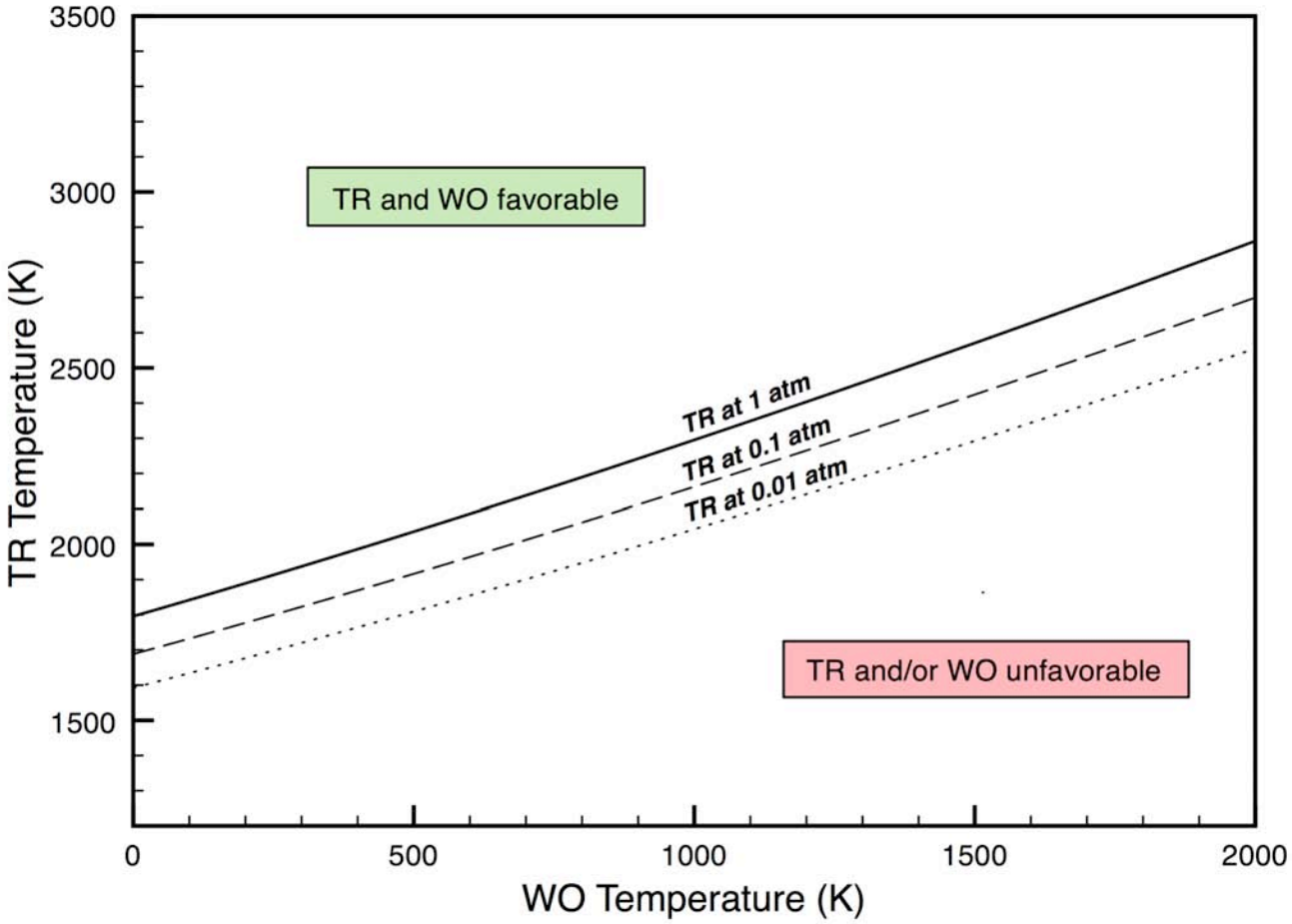

FIG. 1. Temperature and pressure ranges in which TR and WO are thermodynamically favorable, neglecting solid-state entropy (from Eq. 16). The window in which both TR and WO are favorable is restrictive from experimental and materials standpoints.

thermal splitting of H_2O. These conclusions agree with Miller *et al.*'s observations[6] that a large positive TR entropy (mostly provided by O_2) is desirable, and that ΔT=0 implies ΔG_{TR} and ΔG_{WO} must have opposite signs and sum to $\Delta G_f(H_2O)$.

We plot the relationship between thermodynamically allowed T_{TR} and T_{WO} (Eq. 16) in Fig. 1. We find the optimal window for thermodynamics is quite restrictive, especially in light of realistic experimental TR and WO temperatures. This result agrees with previous efforts that found no two-step oxide cycles to be practical below 1373K[21] and the use of three steps to be necessary for any cycle operating below 1000K.[22] We reiterate that this conclusion is independent of the choice of material, and is a simple function of the thermodynamics of H_2O and its constituents. Fig. 1 also indicates the beneficial effects of lowering the TR pressure, which we discuss in more detail below.

In addition to thermodynamic considerations, there are also practical restrictions on the useful temperature ranges which may be considered in a real two-step thermolysis reactor: Materials may be highly volatile or suffer irreversible degradation at very high TR temperatures (>2000K) and kinetic processes will be very slow at very low WO temperatures (<1000K). These practical issues argue for reduced values of ΔT; however, the simple thermodynamic analysis leading to Fig. 1 shows that small values of ΔT are only achievable thermodynamically for very high values of T_{TR} if solid-state entropy is not considered. Though the above analysis is straightforward, one can make strong conclusions about the potential for thermodynamically-preferred two-step reactions for typical oxides at ambient pressure. For instance, the 1atm pressure curve in Fig. 1 comes down to a T_{WO} of 0K at T_{TR} around 1800K. From that, one can conclude (in the absence of solid-state entropy, which we later show for most materials represents an *additional* penalty) that any oxide that has a 1atm equilibrium TR reaction below 1800K can never have an equilibrium-favorable WO reaction at any temperature.

C. Pressure Effects

Eq. 16 is plotted in Fig. 1 for TR pressures of 1atm, 0.1atm, and 0.01atm. Pressure effects can be included by treating oxygen as an ideal gas and simply including a $-R\ln(P)$ term in Eq. 13. Pressure is not expected to play a major role in adjusting the thermodynamics of WO, as gases appear on both sides of the reaction. During TR, however, a partial vacuum can be used to help drive oxygen release,[23] and Figure 1 indicates the magnitude of these pressure effects on the ideal thermodynamic operating window.

D. Effect of Solid-State Entropy

Up to this point, the present analysis has neglected the role of the solid-state entropy difference between the two oxide materials. Returning to Eqs. 9 and 10, and relaxing the entropy assumption, we now introduce another material property (assumed temperature-independent)

$$S^{MO_{x-1}} - S^{MO_x} \equiv \Delta S_{reduction}. \tag{17}$$

Eqs. 9 and 10 then become

$$\Delta G_{TR,T_{TR}} = \Delta H_{reduction} - T_{TR}(\Delta S_{reduction} + \frac{1}{2} S^{O_2}_{T_{TR}}) \le 0 \text{ and} \tag{18}$$

$$\Delta G_{WO,T_{WO}} = -\Delta H_{reduction} - \Delta H^{H_2O}_{f,T_{WO}} - T_{WO}\left(S^{H_2}_{T_{WO}} - S^{H_2O}_{T_{WO}} - \Delta S_{reduction}\right) \tag{19}$$

Similarly, the ΔT expression from Eq. 16 can be modified to include $\Delta S_{reduction}$:

$$\Delta T = \frac{-2\Delta G^{H_2O}_{f,T_{WO}} - T_{WO}\Delta S}{S^{O_2}_{T_{TR}} + 2\Delta S_{reduction}}. \tag{20}$$

Eq. 20 indicates that a positive $\Delta S_{reduction}$ reduces the ΔT needed for favorable TR and WO. However, if $\Delta S_{reduction}$ is negative (as it is in most elemental oxides), it tends to counteract the thermodynamic driving force of O_2 entropy.

The thermodynamically favorable TR-WO temperature window is plotted in Fig. 2 for several constant values of $\Delta S_{reduction}$. The plot demonstrates that large positive values of $\Delta S_{reduction}$ can improve

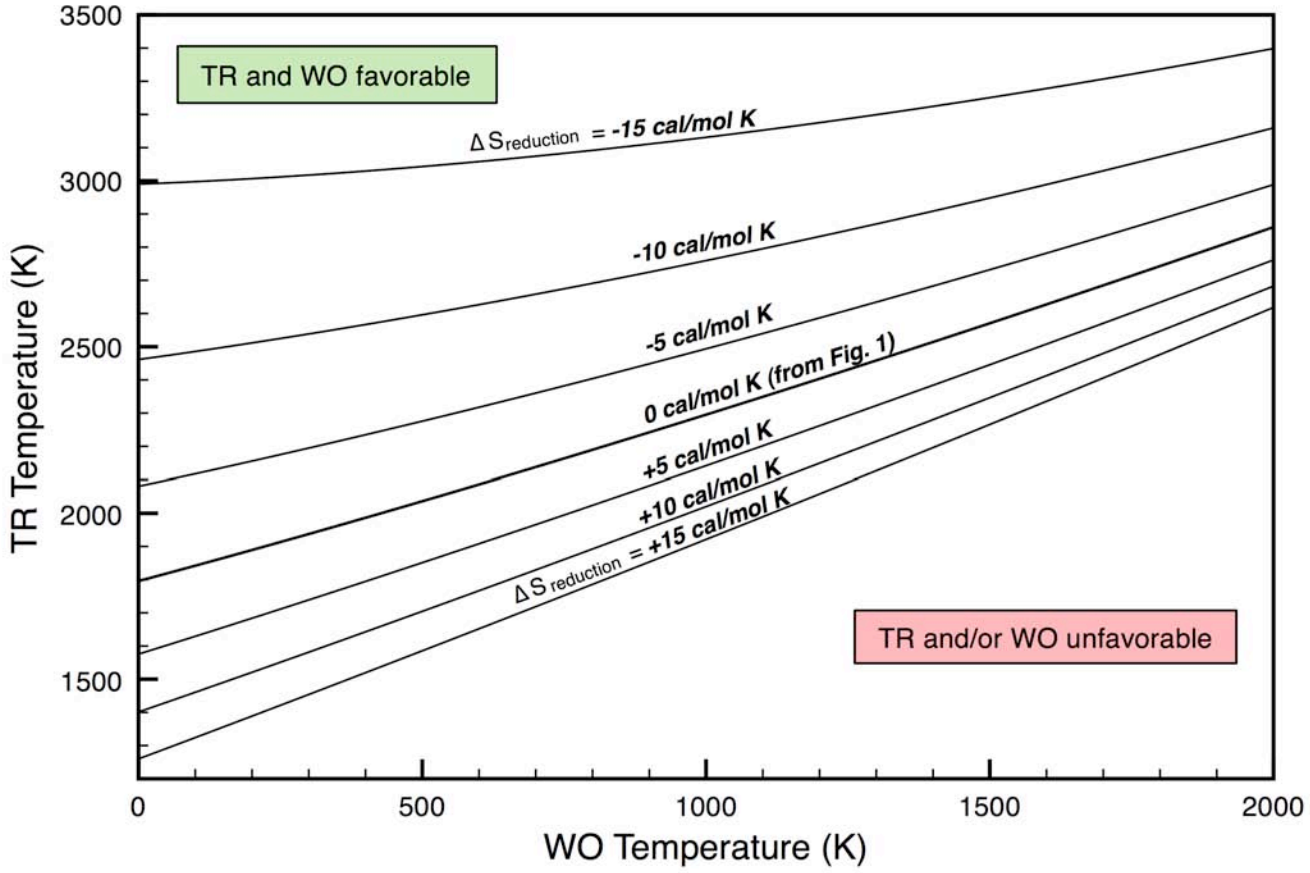

FIG. 2. Temperature ranges in which TR (at 1atm pressure) and WO are thermodynamically favorable, for a set of realistic $\Delta S_{reduction}=S(MO_{x-1})-S(MO_x)$ values. This solid-state entropy delta can, if it is large and positive, broaden the window in which TR and WO are both favorable.

the energetics of a two-step thermolysis cycle. Thus, $\Delta S_{reduction}$ must be considered an important materials design variable along with $\Delta H_{reduction}$.

E. Optimizing the Energetics of TR and WO

The ultimate goal of this analysis is to provide quantitative targets for the ideal thermodynamic properties of oxide materials used in two-step thermolysis cycles. Presently-employed water splitting materials do, of course, function even if one or both steps has unfavorable equilibrium thermodynamics—some product will always be observed regardless of the values of ΔG_{TR} and ΔG_{WO}, and nonequilibrium techniques can push reactions in the desired direction—but lowering ΔG_{TR} and ΔG_{WO} would certainly enhance the cycles' performance. Allendorf *et al.*, for example, discuss both equilibrium considerations and the great importance of non-equilibrium factors in practical solar thermochemical water splitting processes.[10] Here we are concerned with defining the $\Delta H_{reduction}$ and $\Delta S_{reduction}$ regimes that make *both* TR and WO thermodynamically favorable, and then determining whether any binary oxides fall in that window. This ideal window, found by simultaneously satisfying Eqs. 18 and 19, is shown in Fig. 3, along with experimental data for 105 binary oxides.

Among the oxides shown in Fig. 3 are the Fe_3O_4,[3,5,11,13,18] CeO_2,[25] Mn_3O_4,[11,13] Co_3O_4,[11] Nb_2O_5,[11] WO_3,[15] SnO_2,[5] In_2O_3,[5] CdO,[13] and ZnO[5,7,18] cycles that have generated interest in the thermolysis community. Interestingly, these materials are identified as some of the best in our framework: They tend to cluster near the TR and WO equilibrium lines, where neither reaction is excessively penalized in favor of the other. Most also favor WO slightly, which is sensible given that the lower-temperature WO reaction is more likely to suffer from slow kinetics. We conclude that, in general, if one step of the cycle must be thermodynamically unfavorable, the TR reaction should be selected since it will more likely have fast kinetics.

At this point it is important to recognize that until we add specific redox data points to Fig. 3, all steps in our analysis have been entirely general. The material-specific thermodynamic data to which we

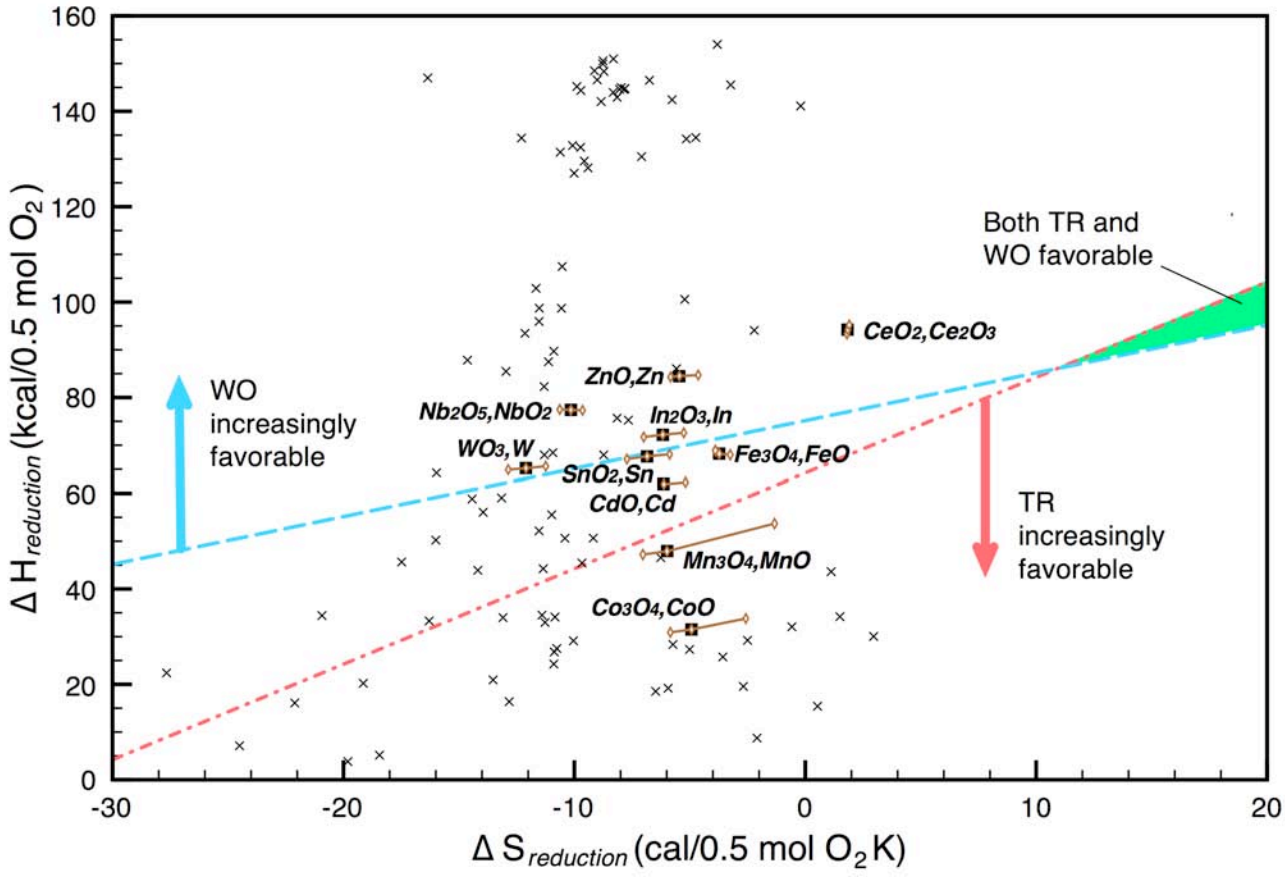

FIG. 3. Regions of favorable TR (below red line) and WO (above blue line) thermodynamics, assuming TR at 2000K and WO at 1000K. Elemental oxide $\Delta H_{reduction}$ and $\Delta S_{reduction}$ values calculated at 1500K (or the next-highest available temperature in 100K increments) from SSUB3 database at 1bar,[20] or, in the case of Fe and its oxides, from NIST.[24] Labeled cycles have generated significant interest in the literature. Brackets on those materials indicate the effects of changing the assumed 1500K temperature by ±200K (exceptions due to limited data: Fe_3O_4 range 1300-1600K, CdO range 1200-1400K, ZnO range 1300-1600K). All the indicated materials except CeO_2 move *left* at higher temperatures.

have access allow us to model TR and WO reactions between stoichiometric line compounds; however, it is a simple matter to include data on this plot for non-stoichiometric systems or solution phases. This possibility is discussed more in the next section. We show in Fig. 3 that *none* of the considered reactions achieve the proper combination of $\Delta H_{reduction}$ and $\Delta S_{reduction}$ needed to enable favorable TR and WO energetics. However, we note that $\Delta S_{reduction}$ serves to open the ideal window for values greater than 10cal/mol.K. Achieving a large positive $\Delta S_{reduction}$ will be nontrivial, since MO_{x-1} has fewer atoms than MO_x (and hence, fewer vibrational degrees of freedom), but Fig. 3 shows that even a few binary oxides already have $\Delta S_{reduction}>0$. An open challenge for the oxide-based water splitting community is to identify or develop materials that possess a large positive $\Delta S_{reduction}$ and also a corresponding $\Delta H_{reduction}$ based on Eqs. 18 and 19. Finally, brackets on select points in Fig. 3 are used to demonstrate the generally very slight temperature dependences of $\Delta H_{reduction}$ and $\Delta S_{reduction}$, corroborating our earlier temperature-independent assumption for these properties.

F. Effects of Off-Stoichiometric Oxides, Solution Phases and Multi-Step Decompositions

Here we comment on the full applicability of our analysis to more complex situations than the reduction and oxidation of stoichiometric line compound oxides. This discussion is motivated by work by Allendorf *et al.*,[10] who considered the thermodynamics of doped ferrite spinel water splitting. Their investigation showed that allowing only the ideal, stoichiometric line compound FeO as a potential decomposition product for Fe_3O_4 led to quantitatively inaccurate predictions of Fe_3O_4 decomposition temperature, and emphasized the significance of including solution phases rather than only line compounds in thermodynamic modeling. We now show that the conclusions of Allendorf *et al.* are compatible with the present analysis.

Throughout this analysis, in keeping with our objective of generality, we do not exclude any potential decomposition products in favor of others. We do not assume in the form of our initial Eqs. 1 and 2 that Fe_3O_4, for example, decomposes strictly to 3FeO during TR. Without altering our framework or its

conclusions, we can write $MO_{x-\delta}$ to represent *any number of compounds or solutions* such that, all together, they are reduced by $\delta/2$ mol O_2 relative to MO_x. Our analysis thus applies to *any* oxygen-evolving step in the potentially complex real-world chain of reactions by which Fe_3O_4 is reduced. One step could, for example, include solution phases via oxygen substoichiometry:

$$Fe_3O_4 \rightarrow Fe_3O_{4-\delta} + \frac{\delta}{2}O_2 \quad . \tag{21}$$

$\Delta H_{reduction}$ and $\Delta S_{reduction}$ will then be functions of δ, but the framework we have developed still applies for each value of δ. Then, once the oxygen solubility limit in Fe_3O_4 is reached at some $\delta_{critical}$, the spinel compound decomposes into a presumably oxygen-rich FeO phase:

$$Fe_3O_{4-\delta_{critical}} \rightarrow 3FeO_{1+\varepsilon} + \frac{\left(4-\delta_{critical}-3-3\varepsilon\right)}{2}O_2 \quad . \tag{22}$$

Clearly, our analysis may still be applied to these more complex and realistic scenarios. Indeed, the only point at which we apply the notion of a stoichiometric line compound approximation is when we add specific materials to Fig. 3 using thermodynamic data. Given such data for any solution phases of interest, those phases could be readily added to the plot as well. Furthermore, if a thermolysis material decomposes by a multi-step pathway, the above results apply to any particular oxygen-producing TR step and its corresponding water oxidation step.

III. Conclusion

In this chemical thermodynamic analysis of oxide-based water splitting, we show that useful general conclusions can be derived for two-step cycles without limiting applicability to a particular material. We found that the quantities $\Delta H_{reduction}$ and $\Delta S_{reduction}$, which represent the enthalpy and entropy differences between reduced (MO_{x-1}) and non-reduced (MO_x) materials participating in thermolysis, together determine the thermodynamic performance of water splitting cycles based on those materials. In the absence of $\Delta S_{reduction}$, only a very large ΔT(>1000K) between the TR and WO steps would give

both steps negative Gibbs free energies of reaction. In most binary oxide redox reactions, $\Delta S_{reduction}$ is negative, and *further* penalizes the water splitting cycle's thermodynamics. However, it is important to note that a material with a very large $\Delta S_{reduction}$ could, if it also had an appropriate $\Delta H_{reduction}$, operate with favorable TR and WO thermodynamics and potentially represent a dramatic improvement over present water-splitting materials. We also observe that any thermolysis cycle, whether or not both steps are favorable, can benefit from reduced TR pressure and non-equilibrium techniques such as sweep gases. Finally, we hypothesize that a cycle with one unfavorable step (the vast majority, at least of the binary oxides) ought to favor WO over TR, since WO is more likely to be kinetically hindered; many of the most widely investigated water-splitting materials today follow this prescription.

Acknowledgment. The authors gratefully acknowledge support from Sandia National Laboratories and the U.S. Department of Energy under LDRD Award No. 752591.

References

(1) Kodama, T. *Progress in Energy and Combustion* **2003**, *29*, 567.

(2) Kogan, A. *International Journal of Hydrogen Energy* **1998**, *23*, 89.

(3) Nakamura, T. *Solar Energy* **1977**, *5*, 467.

(4) Perkins, C.; Weimer, A. *International Journal of Hydrogen Energy* **2004**, *29*, 1587.

(5) Abanades, S.; Charvin, P.; Flamant, G.; Neveu, P. *Energy* **2006**, *31*, 2805.

(6) Miller, J. E.; Allendorf, M. D.; Diver, R. B.; Evans, L. R.; Siegel, N. P.; Stuecker, J. N. *Submitted to Journal of Materials Science* **2007**.

(7) Bilgen, E.; Ducarroir, M.; Foex, M.; Sibieude, F.; Trombe, F. *International Journal of Hydrogen Energy* **1977**, *2*, 251.

(8) Kaneko, H.; Gokon, N.; Hasegawa, N.; Tamaura, Y. *Energy* **2005**, *30*, 2171.

(9) Tamaura, Y.; Steinfeld, A.; Kuhn, P.; Ehrensberger, K. *Energy* **1995**, *20*, 325.

(10) Allendorf, M.; Diver, R.; Siegel, N.; Miller, J. *Submitted to Energy & Fuels* **2008**.

(11) Lundberg, M. *International Journal of Hydrogen Energy* **1993**, *18*, 369.

(12) Palumbo, R.; Lédé, J.; Boutin, O.; Ricart, E. E.; Steinfeld, A.; Möller, S.; Weidenkaff, A.; Fletcher, E.; Bielicki, J. *Chemical Engineering Science* **1998**, *53*, 2503.

(13) Sibieude, F.; Ducarroir, M.; Tofighi, A.; Ambriz, J. *International Journal of Hydrogen Energy* **1982**, *7*, 79.

(14) Sturzenegger, M.; Nuesch, P. *Energy* **1999**, *24*, 959.

(15) Kodama, T.; Gokon, N. *Chemical Reviews* **2007**, 4048.

(16) Licht, S. *ChemComm* **2005**, 4635.

(17) Steinfeld, A. *Solar Energy* **2005**, *78*, 603.

(18) Steinfeld, A.; Kuhn, P.; Reller, A.; Palumbo, R.; Murray, J.; Tamaura, Y. *International Journal of Hydrogen Energy* **1998**, *23*, 767.

(19) Weimer, A.; Francis, T.; Carney, C.; Wyss, J.; Martinek, J.; Kerins, M. *DOE Hydrogen Program FY 2006 Annual Report* **2006**, 216.

(20) Scientific Group Thermodata Europe (SGTE) Substances Database SSUB3.

(21) Funk, J.; Reinstrom, R. *Industrial & Engineering Chemistry Process Design and Development* **1966**, *5*, 336.

(22) Abraham, B.; Schreiner, F. *Industrial & Engineering Chemistry Fundamentals* **1974**, *13*, 305.

(23) Diver, R. B.; Miller, J. E.; Allendorf, M. D.; Siegel, N. P.; Hogan, R. E. *Proceedings of ISEC2006* **2006**.

(24) Chase, M. J. *Journal of Physical and Chemical Reference Data, Monograph 9* **1998**, 1.

(25) Abanades, S.; Flamant, G. *Solar Energy* **2006**, *80*, 1611.

DISTRIBUTION:

5	MS 1349	Eric N. Coker, 01815
1	MS 1411	Mark A. Rodriguez, 01822
1	MS 0734	Andrea Ambrosini, 06338
1	MS 1415	Roland R. Stumpf, 01114
1	MS 0734	Ellen B. Stechel, 06338
1	MS 1349	James E. Miller, 01815
1	MS 9291	Mark D. Allendorf, 08624
1	MS 9052	Anthony H. McDaniel, 08367
1	MS 9409	Daniel E. Dedrick, 08365
1	MS 0734	Chad L. Steiger, 06338
1	MS 0836	Ken S. Chen, 01516
1	MS 0836	Roy E. Hogan, 01514
1	MS 1415	Gary L. Kellog, 01114
1	MS 1127	Nathan P. Siegel, 06337
1	MS 1127	Richard B. Diver, 06337
1	MS 1349	William F. Hammetter, 01815
1	MS 0887	Justine E. Johannes, 01810
1	MS 0887	Duane B. Dimos, 01800
1	MS 1104	Margie L. Tatro, 06200
1	MS 1104	Rush D. Robinett, 06330
1	MS 1110	Jeff S. Nelson, 06337
1	MS 0721	Steve C. Roehrig, 06300
1	MS 0123	LDRD, Donna L. Chavez, 01011
1	MS 0899	Technical Library, 09536 (electronic copy)


Sandia National Laboratories